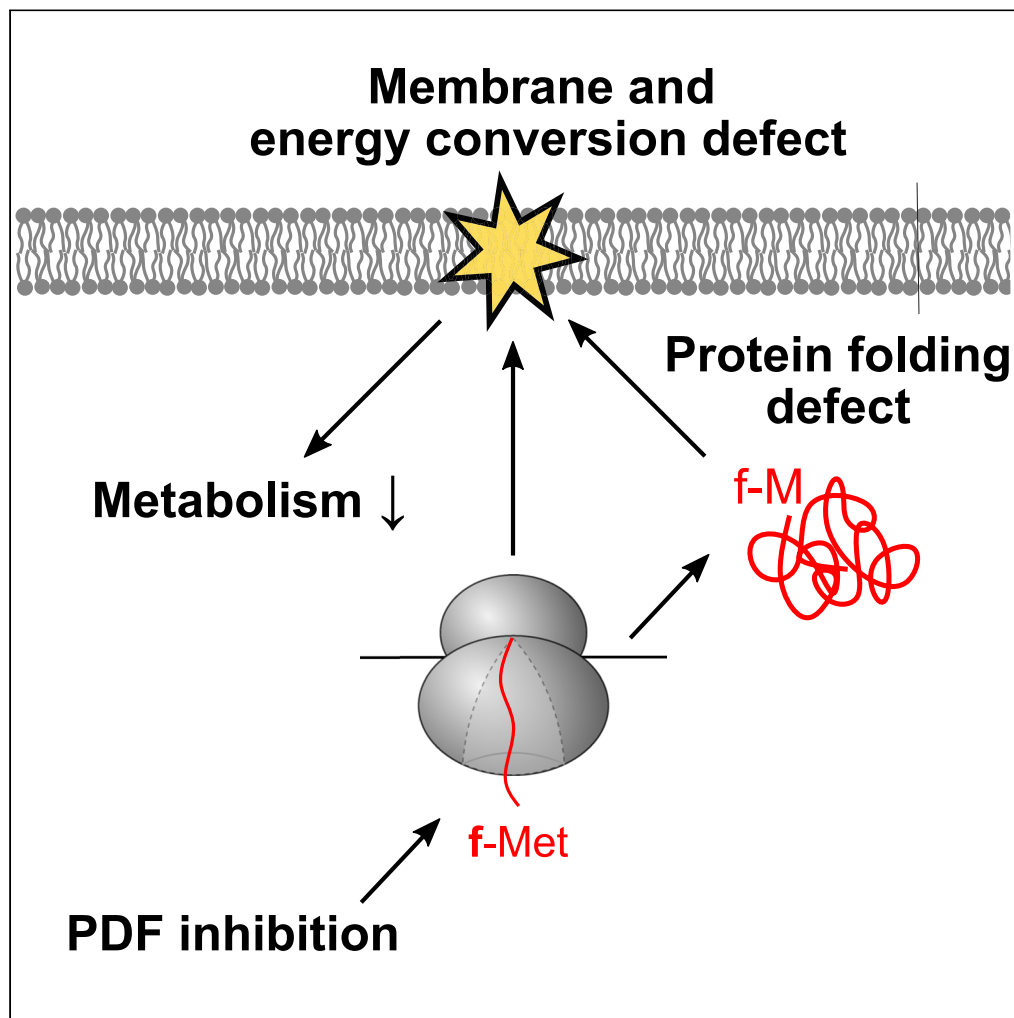**Article**

System-wide analyses reveal essential roles of N-terminal protein modification in bacterial membrane integrity

Chien-I Yang, Zikun Zhu, Jeffrey J. Jones, Brett Lomenick, Tsui-Fen Chou, Shu-ou Shan

sshan@caltech.edu

Highlights

PDF inhibition induces membrane defects and metabolic imbalance

Deformylation is involved in nascent protein folding

Membrane is the earliest and primary target of N-formylation on nascent proteins

PDF activity is essential for redox homeostasis in bacteria

Article

System-wide analyses reveal essential roles of N-terminal protein modification in bacterial membrane integrity

Chien-I Yang,[1] Zikun Zhu,[1] Jeffrey J. Jones,[2] Brett Lomenick,[2] Tsui-Fen Chou,[2] and Shu-ou Shan[1,3,*]

SUMMARY

The removal of the N-terminal formyl group on nascent proteins by peptide deformylase (PDF) is the most prevalent protein modification in bacteria. PDF is a critical target of antibiotic development; however, its role in bacterial physiology remains a long-standing question. This work used the time-resolved analyses of the *Escherichia coli* translatome and proteome to investigate the consequences of PDF inhibition. Loss of PDF activity rapidly induces cellular stress responses, especially those associated with protein misfolding and membrane defects, followed by a global down-regulation of metabolic pathways. Rapid membrane hyperpolarization and impaired membrane integrity were observed shortly after PDF inhibition, suggesting that the plasma membrane disruption is the most immediate and primary consequence of formyl group retention on nascent proteins. This work resolves the physiological function of a ubiquitous protein modification and uncovers its crucial role in maintaining the structure and function of the bacterial membrane.

INTRODUCTION

The synthesis of all bacterial proteins starts with formylated methionine (fMet) (Adams and Capecchi, 1966; Gualerzi and Pon, 1990). Following translation initiation, the formyl group on nascent polypeptides can be removed cotranslationally by peptide deformylase (Adams, 1968; Giglione et al., 2004) (PDF, encoded by *the def* gene in *Escherichia coli*). PDF is a promiscuous enzyme with limited specificity and affects up to 90% of the proteome, rendering deformylation as the most prevalent N-terminal modification in bacteria (Adams, 1968; Bienvenut et al., 2015; Meinnel et al., 1993; Ragusa et al., 1999). Consistent with its ubiquitous activity, deformylation is an essential process in bacteria, as evidenced by the lethality of *def* knockout (Mazel et al., 1994). Thus, PDF has been a prominent target for developing efficient and specific antibiotics (Giglione et al., 2000). Despite the early discovery and importance of PDF, it remains unclear why it is essential for bacterial survival. Methionyl-tRNA formyltransferase (MTF, encoded by the *fmt* gene), which delivers the formyl group to methionine, enhances the efficiency and specificity of translation initiation but is dispensable (Antoun et al., 2006; Guillon et al., 1992; Sundari et al., 1976). Interestingly, the additional knockout of *fmt* rescues the growth of Δ*def* cells (Margolis et al., 2000; Mazel et al., 1994). Analogously, mutations in genes involved in the generation of fMet-tRNA^{fMet} confer resistance to PDF inhibitors (Duroc et al., 2009). These observations indicate that the retention of fMet on proteins is detrimental to the cells.

It is also unknown how PDF activity affects protein function and cellular processes. Traditionally, the requirement for PDF is attributed to another essential enzyme, methionine aminopeptidase (MAP, encoded by the *map* gene) (Ben-Bassat et al., 1987; Giglione et al., 2000), which catalyzes N-terminal methionine excision (NME) after the action of PDF on ∼50% of bacterial proteins (Frottin et al., 2006; Hirel et al., 1989; Solbiati et al., 1999). MAP is universally conserved and plays crucial roles in multiple cellular processes in higher eukaryotic organisms, including angiogenesis, cell cycle, translation, and glutathione metabolism (Frottin et al., 2009; Fujii et al., 2018; Giglione et al., 2004; Griffith et al., 1998; Hu et al., 2006). In bacteria, MAP is required for cell viability (Chang et al., 1989), but its role in bacterial physiology is equally elusive. Multiple hypotheses have been proposed to explain the essentiality of MAP (Giglione et al., 2004, 2015; Meinnel et al., 1993). First, MAP may be involved in the metabolism of methionine, one of the most expensive amino acids for *de novo* synthesis by cells (Old et al., 1991). This model is supported by the induction of the Met biosynthesis pathway upon the inhibition of the *map1* gene in yeast (Dummitt et al., 2003),

implicating a role of MAP in Met recycling. Whether such Met salvage pathway is essential in bacteria remains to be tested. Second, some essential proteins may require fMet removal to acquire activity (Meinnel et al., 1993), such as N-terminal hydrolases that use an N-terminal Ser, Cys or Thr as the nucleophile. However, there is limited knowledge of such NME-dependent proteins to date, few of which have been reported in *E. coli* (Brannigan et al., 1995; Kim et al., 1996; Larsen et al., 1999; Mouilleron et al., 2006; Oinonen and Rouvinen, 2000; Park et al., 2008; Yoo et al., 1997).

A different model for the role of fMet is suggested from comparison with a chemically similar modification in eukaryotes, N-terminal acetylation. Appendage of the formyl or acetyl group to the N-terminal amine reduces the net charge at the N-terminus and adds a potential interaction site to nascent proteins. N-terminal acetylation can contribute to the folding and function of multiple proteins by stabilizing secondary structures at the N-terminus (Greenfield et al., 1994; Jarvis et al., 1995; Kang et al., 2012), to protein-protein interactions by preventing the repulsion of the charged N-terminus or establishing additional contacts (Scott et al., 2011; Singer and Shaw, 2003), and to protein half-life by providing a 'degron' for the Ac/N-end rule pathway (Hwang et al., 2010; Varshavsky, 2019). Analogous roles could be envisioned for the N-terminal formyl group. Indeed, both the formyl group and the initiator Met have been proposed to control the protein half-life via the bacterial fMet/N-degron and Leu/N-degron pathways, respectively (Ninnis et al., 2009; Piatkov et al., 2015; Tobias et al., 1991; Varshavsky, 2019), as evidenced by fMet-dependent degradation of model substrates in *E. coli* (Piatkov et al., 2015) and by the initiator methionine-dependent recruitment of the ClpS-ClpAP protease machinery to putrescine aminotransferase (Ninnis et al., 2009). However, the native substrates of bacterial N-degron pathways are poorly characterized (Schmidt et al., 2009). The extent to which fMet affects the proteome via the regulation of protein stability and/or other aspects of protein biogenesis and function is unclear.

This work aims to fill the knowledge gap between the biochemical activity and physiological significance of PDF by studying the effects of its inhibition using system-wide analyses of the translatome and steady-state proteome. The acute disruption of PDF function was found to induce protein folding defects and membrane stress responses, leading to the perturbation of cellular bioenergetics and a wide range of metabolic pathways. Importantly, the time-resolved analyses of cellular responses to PDF inhibition revealed the early onset of membrane hyperpolarization and membrane-associated defects, suggesting the membrane as an immediate and primary target of fMet-retaining nascent proteins.

RESULTS

Effect of PDF inhibition on the bacterial proteome

We reasoned that cells could detect and respond to defects in physiologically essential processes caused by the loss of PDF function. To investigate these cellular responses, we measured the changes in the steady-state bacterial proteome upon PDF inhibition. To rapidly inactivate PDF, we used the antibiotic actinonin (ACT), which reversibly and specifically binds the PDF active site with nanomolar affinity (Chen et al., 2000; Fieulaine et al., 2011; Van Aller et al., 2005) and causes fMet retention on nascent proteins *in vivo* (Bienvenut et al., 2015). The *E. coli* strain CAG12184, in which the multidrug exporter *tolC* was inactivated (Bienvenut et al., 2015; Singer et al., 1989), was used to facilitate the ACT treatment. Unless otherwise specified, CAG12184 cells were grown in a defined medium with a doubling time of 70–90 min and were continuously replenished with fresh medium upon entering the mid-log phase to minimize other sources of stress, such as saturation and nutrient depletion. Upon treatment with 4 μg/mL ACT (16-fold of minimal inhibition concentration (Chen et al., 2000)), cells continued to grow exponentially for ~2 generations before exhibiting a growth defect, and growth stopped after ~9 h (Figure 1A), consistent with the bacteriostatic effect of ACT and the essentiality of PDF (Chen et al., 2000; Mazel et al., 1994).

To enable the quantitative assessment of the proteome, we used Stable isotope labeling by amino acids in cell culture (SILAC) coupled to Tandem mass tags (TMT), which allows the sensitive and efficient analysis of multiplexed samples by LC-MS/MS (Welle et al., 2016). Cells grown in the presence of light and heavy amino acids in a defined medium were treated with 4 μg/mL of ACT and mock-treated, respectively. At 0, 1.5, 4.5, and 9 h after ACT treatment, an equal amount of protein from ACT-treated and control cells were mixed, protease-digested, and labeled with TMTpro16 reagents, which allowed the simultaneous identification and quantification of samples from the four time points in four biological replicates using LC-MS/MS (Figure 1B). In total, we quantified the time-dependent changes in the abundance ratio of 1,932 proteins (Figure S1A and Table S1). We searched for and quantified the N-formylated peptides to verify PDF inhibition in an independent SILAC
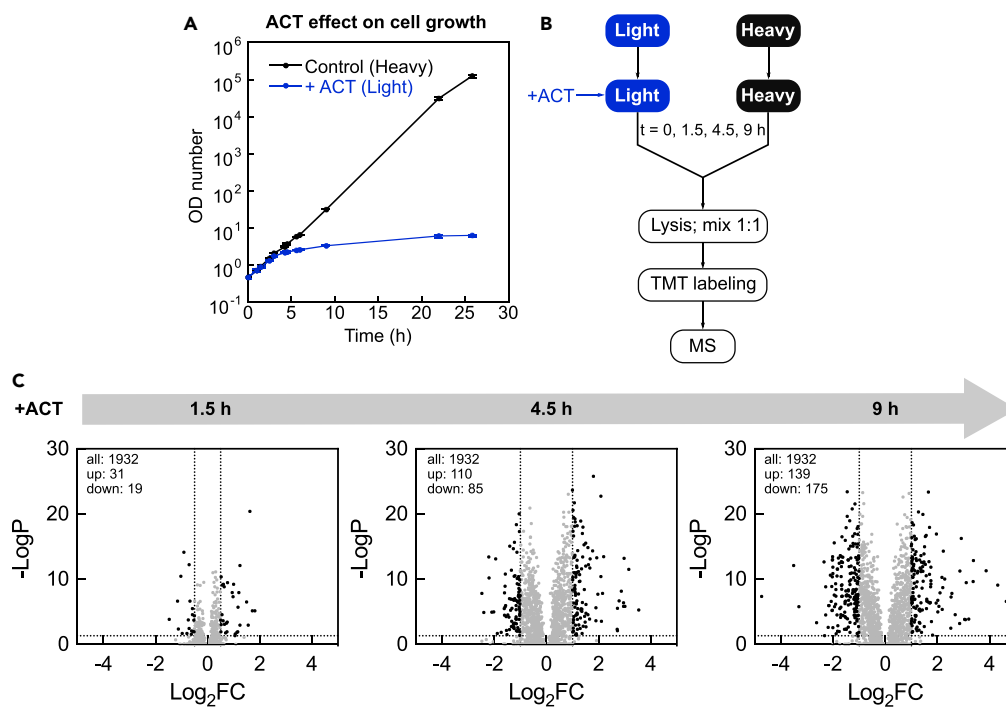
Figure 1. Inhibition of PDF activity leads to time-dependent changes in *E. coli* proteome

(A) Growth curve of CAG12184 cells in SILAC medium in the absence and presence of 4 μg/mL actinonin (ACT). Cell cultures were diluted with fresh medium when they reached mid log phase (OD_{600} = 0.4–0.7). OD number is defined as the product of measured OD_{600} value and the dilution factor. Values are shown as mean ± SD, with n = 3. Error bars are shown but may not be visible.

(B) Overview of the SILAC-TMT procedures for proteomic analysis of PDF inhibition. Cell lysates from the light (ACT-treated) and heavy (untreated) culture collected at the indicated times were mixed at 1:1 protein ratio, digested, labeled with TMT reagents and analyzed by LC/MS.

(C) Volcano plots of the fold change (FC) in protein abundance upon ACT treatment. FC is defined as the ratio of the time-dependent protein level change between the light and heavy channels, as described in STAR Methods. Significantly up- and down-regulated proteins ($|\log_2 FC| \geq 0.5$ for 1.5 h and $|\log_2 FC| \geq 1$ for 4.5 and 9 h, adjusted p $\leq$ 0.05) are highlighted.

experiment. The averaged peptide N-formylation reached ∼40% at 1.5 h and ∼60% after 4.5 h of ACT treatment (Figure S1B), comparable to a previous study (Bienvenut et al., 2015).

Differential expression analysis demonstrated increasing proteome changes over time (Figure 1C and Table S1). The analysis of the significantly up- or down-regulated proteins using the DAVID annotation clustering algorithm (Huang et al., 2007, 2009; Jiao et al., 2012) revealed the enrichment of distinct cellular pathways at different stages after PDF inhibition (Figure 2A; Table S2). At 1.5 h, the iron-sulfur (Fe-S) biogenesis pathway and stress responses, including the cold shock response and phage shock response pathways, were enriched in the up-regulated proteins. At 4.5 h, when growth defects begin to manifest in ACT-treated cells, translation and transcription-related proteins were up-regulated, along with the down-regulation of secretory proteins. Late responses to ACT treatment observed at 9 h included the down-regulation of metabolic pathways for thiamine, amino acids, and glutathione (Figure 2A). In addition, proteins involved in multiple metabolic pathways, including respiration and nucleotide/lipid biosynthesis, were differentially expressed (Table S2 and Figure 2B). The regulated proteins were mapped to a manually curated pathway network, allowing us to assess the spatial, temporal, and biochemical connections between the different responses (Figure 2B).

Effect of PDF inhibition on the bacterial translatome

The observed steady-state proteome responses to PDF inhibition could be attributed to changes in protein synthesis and/or degradation. To distinguish between these possibilities and complement the proteomic analysis, we used ribosome profiling (Ingolia et al., 2012) to investigate the system-wide perturbation of
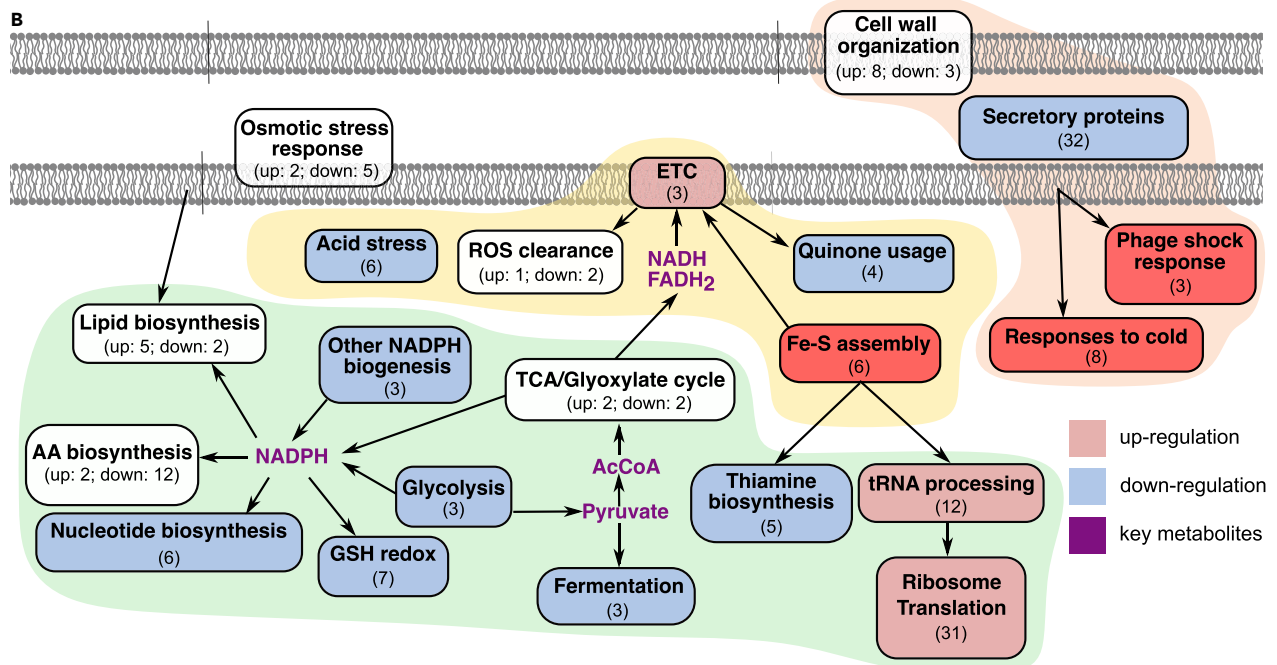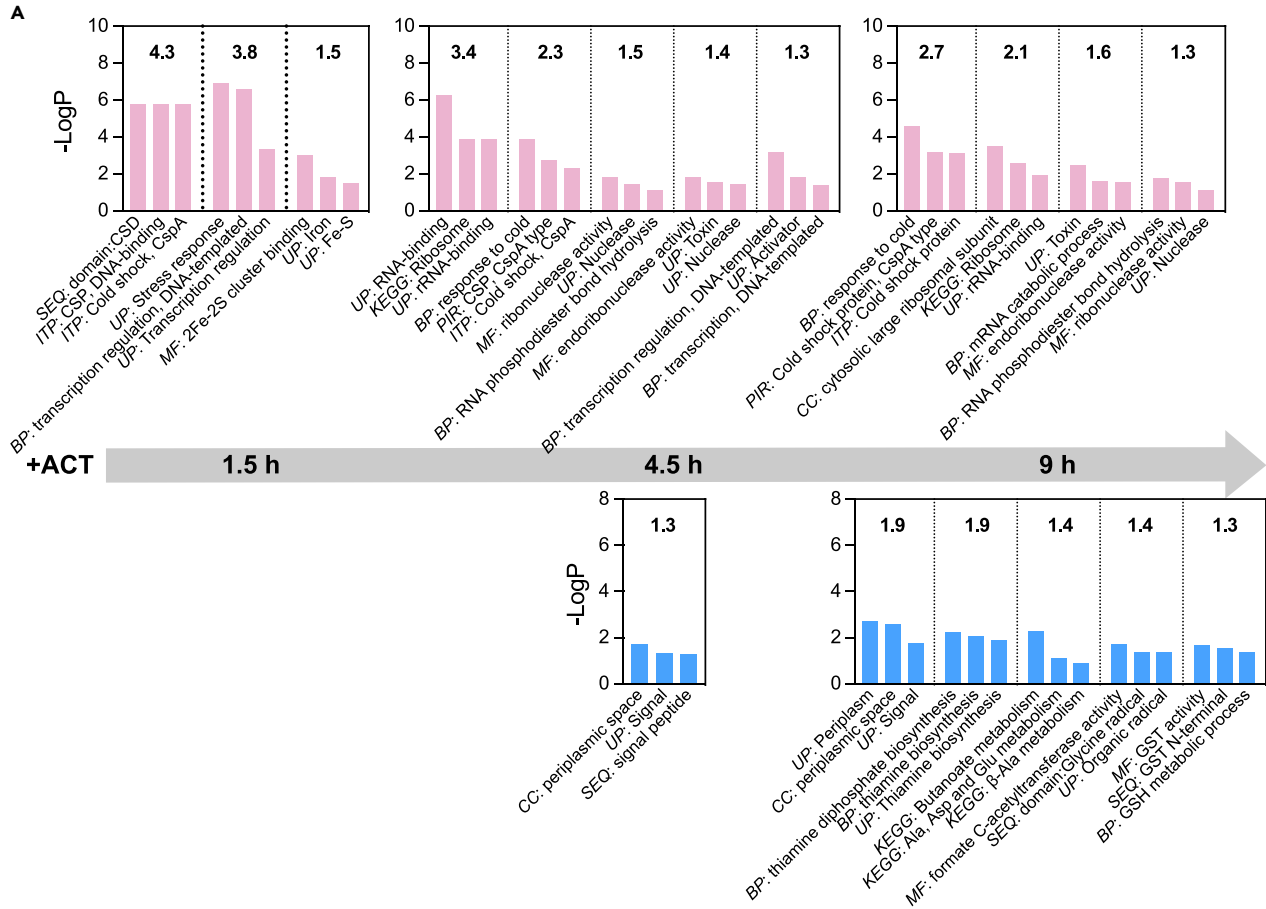
Figure 2. Overview of proteomic changes induced by PDF inhibition

(A) Enrichment analysis of differentially expressed proteins upon PDF inhibition. Up- or down-regulated proteins, as defined in Figure 1C, were subjected to DAVID functional annotation clustering using annotation terms from GO Biological process (labeled as *BP*), GO Molecular function (*MF*), GO Cellular component (*CC*), Uniprot Keywords (*UP*), Uniprot Sequence Features (*SEQ*), Kegg Pathway (*KEGG*), Inter-Pro (*ITP*), PIR Super-Family (*PIR*) and SMART (*SM*). Significant clusters (Enrichment Score (indicated in bold) ≥ 1.3) among the up-regulated (red) and down-regulated (blues) proteins are shown with the top three annotation terms and their P-values in each cluster.

(B) The regulated proteins, as defined in Figure 1C, are manually mapped to the cellular pathway network. Up- and down-regulated pathways are colored in red and blue, respectively, with the total number of regulated proteins indicated in parentheses. Darker colors indicate pathways in which ≥50% of the regulated proteins are observed at 1.5 h. Pathways containing both up- and down-regulated proteins are not colored. Pathways involved in membrane function (peach), bioenergetics (yellow), and metabolism (green) are color-shaded.

the translatome, which includes changes at the transcriptional and translational levels. Notably, the sensitivity of ribosome profiling allows us to explore the early cellular events in direct response to PDF inhibition. To this end, ribosome-protected mRNA footprints were isolated from cells before or after 0.25, 0.5, and 1.5 h of ACT treatment and subjected to deep sequencing. The gene-wise expression level was determined by the sum of normalized reads (RPM) at each codon across the transcript. From three consistent biological replicates, we quantified the time-dependent translational profile of 2,405 genes (Figure S2A and Table S3).

Differential expression analysis of the translatome data revealed significant changes in protein synthesis as early as 0.25 h after PDF inhibition, with 37 and 27 genes up- and down-regulated by more than twofold, respectively, and the changes became more pronounced after 1.5 h (Table S3 and Figure 3A). The changes in the translatome correlated well with the steady-state proteome changes after 1.5 h of ACT treatment, suggesting that the observed perturbation in the proteome arises primarily from the regulations of protein synthesis instead of degradation (Figure S2B). DAVID clustering analysis on the genes differentially expressed by more than twofold (*p* < 0.05) revealed the enrichment in several pathways observed in the proteomic analysis, including the up-regulation of various membrane proteins and the translation machinery and the down-regulation of secretory proteins and glutathione metabolism at 1.5 h (Table S4 and Figure 3B). Multiple metabolic pathways were enriched in the down-regulated translatome, including the TCA cycle, glycolysis, and the biosynthesis of nucleobases and amino acids (Table S4 and Figure 3B). Notably, an up-regulation of the heat shock response was observed at 0.25 h of ACT treatment, indicating an immediate response to PDF inhibition (Table S4 and Figure 3B). Compared with the proteomic data, the ribosome profiling results detected earlier and more prominent changes in gene expression in diverse cellular pathways (Figure 3C). This outcome reflects the higher sensitivity of the ribosome profiling technique. It suggests the presence of rapid cellular adaptive responses to PDF inhibition before changes in steady-state protein abundance are detected (Figures 5, 6, S4, and S7–S9 below).

Collectively, both the proteome and translatome analyses reveal extensive ACT-induced perturbations in diverse cellular pathways, consistent with the ubiquitous action of PDF across the proteome. Mapping the proteome and translatome perturbations to the network of biochemical pathways suggests that PDF inhibition caused changes in the expression of genes involved in several related cellular processes: protein folding; structure and function of the cellular membrane; bioenergetics at the membrane; and redox-dependent metabolic pathways (Figures 2B and 3C). These changes are described and biochemically tested in the following sections.

Retention of fMet induces protein misfolding

One of the earliest stress responses to PDF inhibition is the increased translation of multiple heat shock response proteins, including the Hsp70 chaperone system DnaK/J/GrpE, the Hsp90 chaperone HtpG, the small heat shock protein IbpA, the chaperonin GroEL-GroES, the disaggregase ClpB, and the proteases HslU/V and Lon (Figures 3B, 3C, and 4A). The synthesis of these chaperones and quality control types of machinery increased more than two fold after 15 min of ACT treatment, followed by a decline in their translation and steady-state protein levels over time, strongly suggesting an immediate and transient protein folding stress upon PDF inhibition. To test this model, we pulse-labeled the proteins synthesized after ACT treatment for 0.5 h using ^{35}S-methionine and cysteine and isolated protein aggregates using adaptations of an established protocol (Friedrich et al., 2021; Tomoyasu et al., 2001). We observed an ~40% increase in detergent-insoluble protein aggregates in cells treated with both ACT and MG132, a HslU/V inhibitor (Park et al., 2008; Rohrwild et al., 1996) (Figures 4B, 4C, and S3). Thus, failure to remove the N-terminal formyl group could disrupt the folding of newly synthesized proteins, which are subjected to quality control by the HslU/V protease complex.
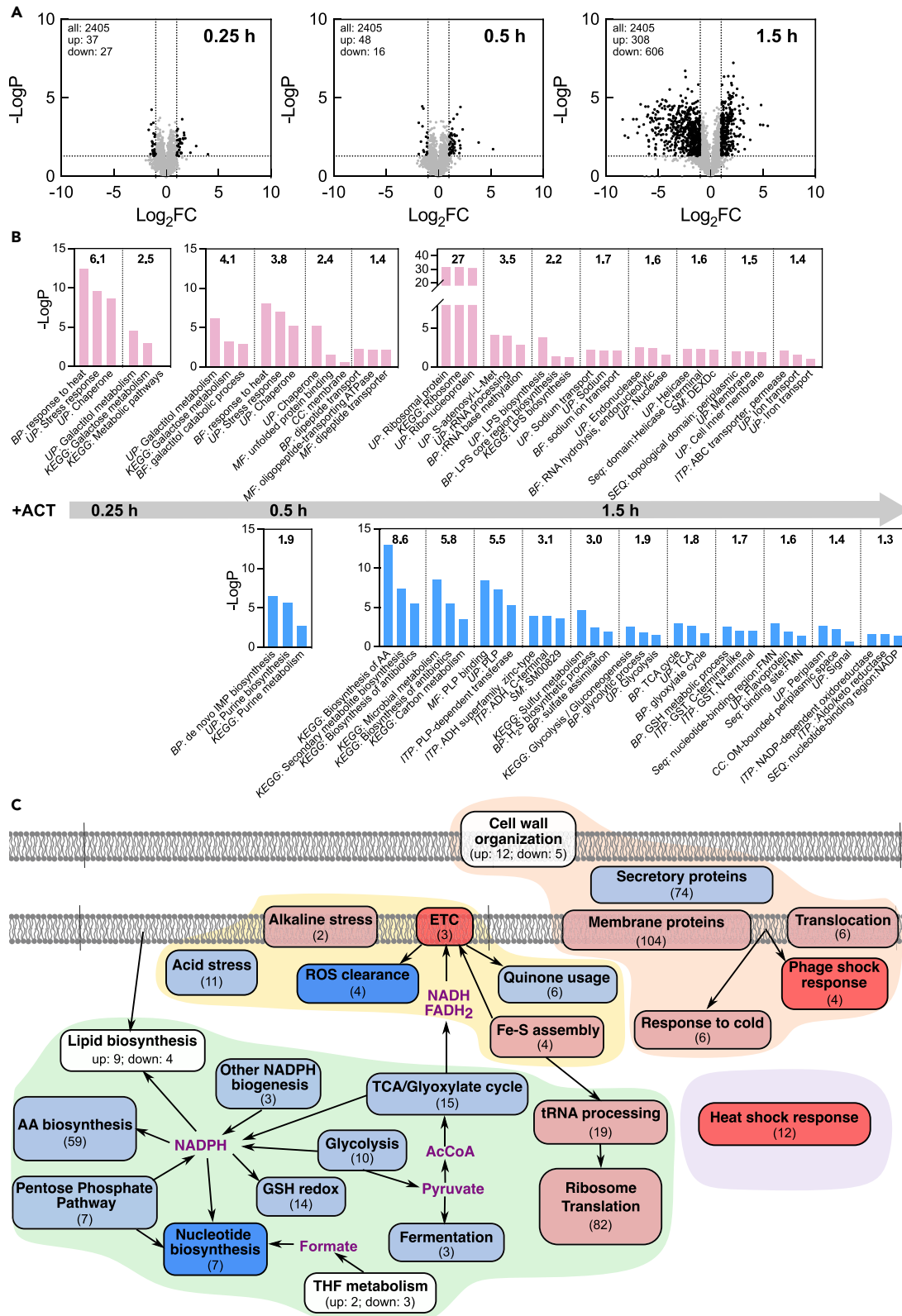
Figure 3. Effect of PDF inhibition on bacterial gene translation

(A) Volcano plots of the fold change (FC) in translation level upon ACT treatment, determined by ribosome profiling. The thresholds for up- or down-regulated genes ($\log_2$FC $\geq$ 1 or $\leq$ −1, p < 0.05) are indicated.

(B) Enrichment analysis of differentially translated proteins upon PDF inhibition. Up- or down-regulated genes were subjected to DAVID functional annotation clustering. Annotation categories are abbreviated as described in Figure 2B. Significant clusters (Enrichment Score $\geq$1.3) among the up-regulated (red) and down-regulated (blues) genes are shown with the top three annotation terms and their P-values in each cluster.

(C) The regulated genes, as defined in (A), are manually mapped to the cellular pathway network. Up- and down-regulated pathways are colored in red and blue, respectively, with the total number of regulated genes indicated in parentheses. Darker colors indicate pathways in which $\geq$50% of the regulated genes are observed at 0.25–0.5 h. Pathways containing both up- and down-regulated genes are not colored. Pathways involved in protein folding (purple), membrane function (peach), bioenergetics (yellow), and metabolism (green) are color-shaded.

PDF inhibition causes defects in the bacterial membrane

Genes involved in stress responses associated with the bacterial membrane comprise a significant cluster of ACT-induced changes (Figures 2B and 3C, shaded in peach). The up-regulation of major components in the phage shock (Psp) and cold shock (Csp) response pathways, including PspA/B/C and CspA/B/G, are among the most pronounced proteome responses to PDF inhibition (Table S1). In addition, the translation of PspA/B/C increased by more than twofold as early as 0.25 h (Figures 3C and 5A). The Psp system is usually induced upon exposure to membrane stress to protect the integrity of the bacterial inner membrane. The induction of cold shock proteins often accompanies a change in membrane fluidity (Barria et al., 2013; Flores-Kim and Darwin, 2016; Jovanovic et al., 2014). The up-regulation of these stress pathways strongly suggests immediate membrane defects upon PDF inhibition.

Following the onset of membrane stress responses, at 1.5 h in the translatome and 4.5–9 h in the steady-state proteome, we observed a decrease in the translation and abundance of multiple secretory proteins and an increase in the translation of membrane proteins, including components of all the major protein translocation machinery, such as SecYEG/DF, YidC, and Tat (Figure S4), suggesting compromised protein translocation at the bacterial inner membrane. Multiple cell wall generation and maintenance proteins were also dysregulated (Figures 2B and 3C). Similar to cells deficient in the membrane protein targeting factor, signal recognition particle (Zhang et al., 2012), cells subjected to prolonged PDF inhibition exhibited elongated and heterogeneous morphology (Figures S5A–S5C).

To directly test the effect of PDF inhibition on the bacterial membrane envelope, we measured the susceptibility of cells to SDS, which induces lysis more readily when the cell envelope is compromised (Singh et al., 2021; Zhang et al., 2012). Cells exhibited increased sensitivity to SDS after 40 min of ACT treatment. This effect was exacerbated after 120 min of treatment, at which 50% of ACT-treated cells were lysed by 0.05% SDS within 10 min, whereas >80% of mock-treated cells remained intact (Figures 5B and S5D–S5G). In addition, we measured the integrity of the inner membrane using a fluorescent probe, propidium iodide (PI), which penetrates the permeabilized membrane to bind the DNA (Stocks, 2004; Sträuber and Müller, 2010). We observed a significant increase in PI fluorescence after 5 h of ACT treatment, indicative of substantial membrane rupture (Figure 5C). Cells grown in a rich medium exhibited similar albeit earlier membrane defects, potentially owing to more active protein translation. Under the same growth condition, the membrane of cells lacking formyltransferase (Δfmt (Piatkov et al., 2015)), which bypasses deformylation, remained intact even after 6 h of ACT treatment (Figure S5H). These observations rule out the off-target effects of ACT and suggest a direct role of formylated nascent proteins in disrupting the bacterial membrane's integrity.

PDF inhibition disturbs bioenergetics at the membrane

In addition to the membrane-associated stress responses, iron-sulfur cluster (Isc) biosynthesis factors and chaperones (IscU/R/S/X and HscA/B) and the Fe-S cluster carrier ErpA are enriched in the earliest up-regulated proteome at 1.5 h (Figures 2 and 6A). An increased translation of components of these pathways was observed beginning at 0.5 h (Figures 3C and 6A). In addition, we observed an increase in the translation and steady-state level of multiple Fe-S cluster-binding enzymes, including several enzymes involved in tRNA processing (TtcA and MiaB) and the subunit of electron transport chain (ETC) complex II (SdhB) (Figures 2B, 3C, and 6A), consistent with the essential role of the Isc pathway in the maturation of Fe-S enzymes (Ezraty et al., 2013).

The translation of other subunits of ETC complex II (SdhA, SdhC) and the steady-state level of the ETC complex I subunit NuoC were also up-regulated (Figures 2B, 3C, and 6A), suggesting a disturbance in oxidative
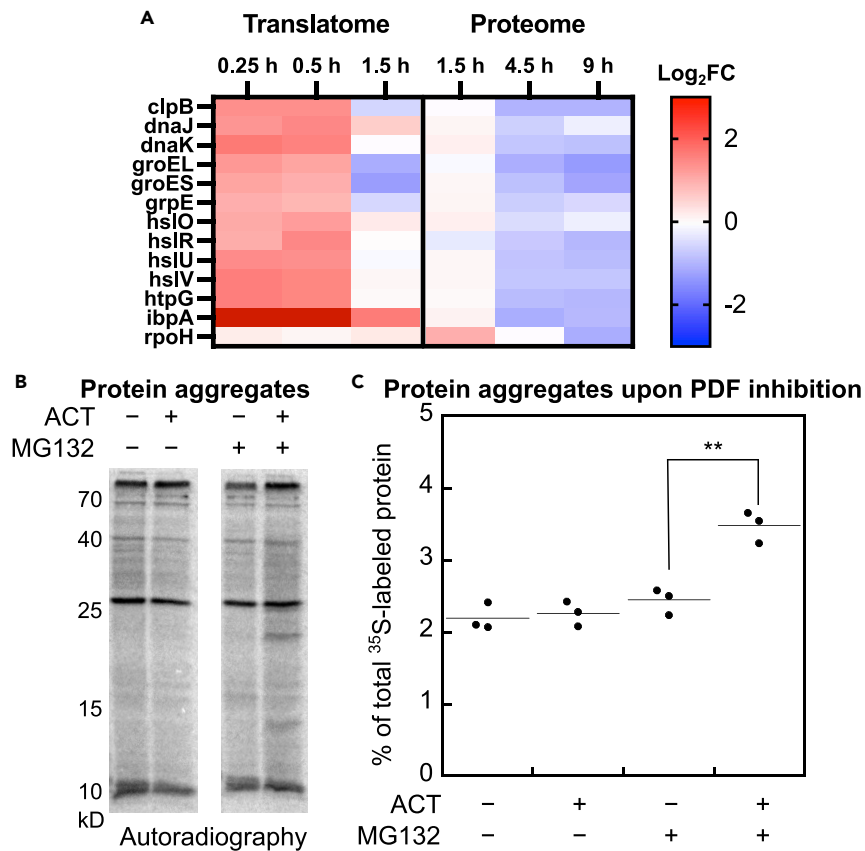
Figure 4. PDF inhibition induced protein folding stress

(A) Time-dependent changes (log$_2$FC) in the translation (left) and steady-state protein level (right) of heat shock response genes upon PDF inhibition.

(B) Representative autoradiographs of the analysis of nascent protein aggregates. Where indicated, cells were treated with ACT (4 μg/mL) and/or MG132 (20 μM) in the presence of ^{35}S-methionine/cysteine for 30 min. Detergent-insoluble protein aggregates were isolated and analyzed by autoradiography. The original gel image including the total and different fractions of the nascent proteins are shown in Figure S3.

(C) Quantification of ^{35}S-labeled protein aggregates isolated from cells treated with the indicated compounds. Data were analyzed by autoradiography and are shown as mean with the values from three biological replicates displayed. **: p < 0.01.

phosphorylation that couples redox energy to the generation of proton motive force (PMF). Related to these observations, a significant down-regulation of acid stress response was detected at 1.5 h of ACT treatment, including components of the glutamate-dependent acid resistance (AR2) system (GadA/B/C/E/X) that consume intracellular protons via the decarboxylation of glutamate (Foster, 2004; Krulwich et al., 2011) (Figures 2B, 3C, and 6A, cluster III). In contrast, the translation of NhaA and NhaB, which export Na$^+$ in exchange for protons during alkaline stress (Padan et al., 2005), was up-regulated at 1.5 h (Figures 3C and 6A). These observations suggest that the cells respond to PDF inhibition by increasing the proton concentration at the cytosolic side of the plasma membrane. Several genes involved in response to reactive oxygen species (ROS) and the consumption of quinone were also differentially regulated in the translatome and proteome data (Figures 2B and 3C). Together, these observations suggest that PDF inhibition leads to abnormal bioenergetics at the plasma membrane.

To directly test this hypothesis, we used a Nernstian voltage indicator, thioflavin T (ThT), to measure the membrane potential (Δψ) component of PMF upon PDF inhibition (Prindle et al., 2015). Cationic ThT molecules permeate the cell and accumulate on the cytoplasmic side of the membrane owing to the negative membrane potential, giving rise to increased fluorescence signals (Figure 6B) (Prindle et al., 2015). Treatment with carbonyl cyanide *m*-chlorophenyl hydrazone (CCCP), a protonophore that depolarizes the cell,
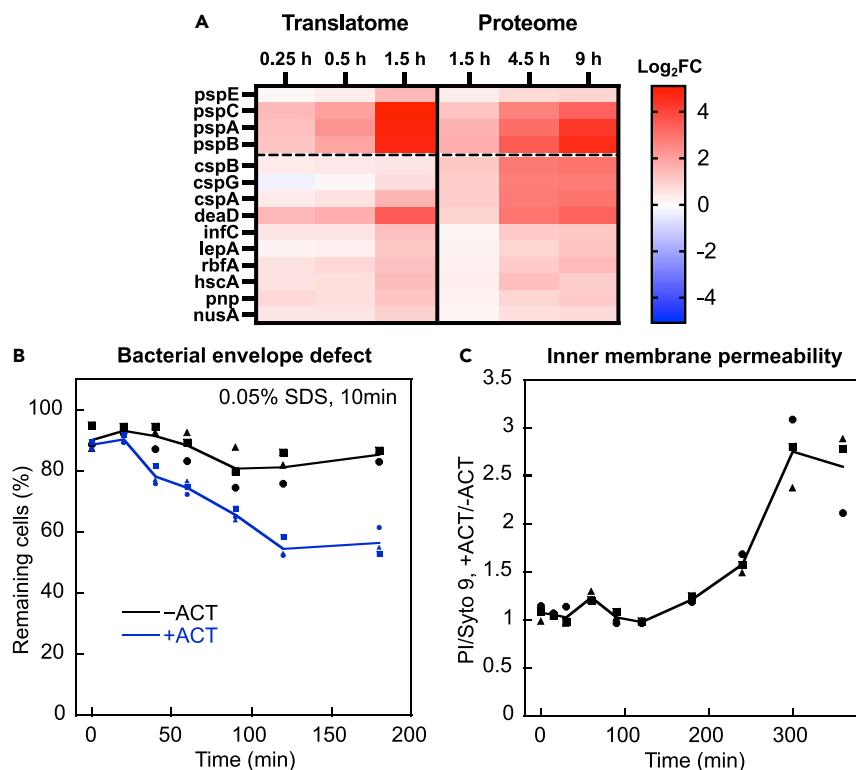
Figure 5. PDF inhibition leads to bacterial membrane defect

(A) Time-dependent changes (log$_2$FC) in the expression (left) and steady-state protein (right) level of indicated phage shock genes (top) and genes related to cold response (bottom) upon PDF inhibition.

(B) SDS susceptibility of cells upon PDF inhibition. After ACT addition, CAG12184 cells collected at the indicated times were mixed with 0.05% SDS. The cell density was determined by OD$_{600}$ after 10 min and normalized to that before SDS addition. The data for three biological replicates are shown, and the line represents the mean.

(C) The effect of PDF inhibition on the inner membrane integrity of CAG12184 cells. The membrane permeability was measured by the ratio of fluorescence intensity of propidium iodide (PI) to the membrane permeable dye Syto nine and normalized to that of the cells without ACT treatment. The values for three biological replicates are shown, and the line represents the mean.

abolished the fluorescence (Figure 6B). We observed a drastic increase in ThT fluorescence upon PDF inhibition, which was detected as early as 15 min after ACT treatment and continued to rise until 90 min when it reached the maximum detectable value (Figure 6C), indicating an extensive membrane hyperpolarization (Figures 6B and 6C). In contrast, the membrane potential of Δ*fmt* cells remained invariant (Figure S6A). Independent measurements with another established membrane potential indicator DiOC$_2$ (3), exhibiting a red shift in emission wavelength (Hudson et al., 2020; Novo et al., 1999) and confirming the ACT-induced hyperpolarization detected by ThT (Figure S6B). Notably, the addition of CCCP abolished the ACT-induced ThT signal, excluding other factors that could enhance ThT fluorescence, such as protein aggregation (Figure S6C). Finally, the additional presence of a translation inhibitor, chloramphenicol, rescued the ACT-induced membrane hyperpolarization, suggesting that the observed changes in membrane potential are directly caused by the retention of the formyl group in newly synthesized proteins (Figure S6D). Collectively, these observations demonstrate that the accumulation of fMet-retaining nascent proteins induces rapid membrane hyperpolarization and disruptions of membrane bioenergetics.

PDF inhibition disrupts metabolism and redox homeostasis

Multiple metabolic pathways were also dysregulated following PDF inhibition. At 0.5 h following ACT treatment, we observed reduced translation of genes involved in the *de novo* biosynthesis of pyrimidine and purine (Figures 3C and S7A). This action could be partially attributed to the inhibition of NME on amidophosphoribosyl transferase (purF), which requires the unmasking of Cys2 to catalyze a committed step in *de novo* purine synthesis (Kim et al., 1996). Alternatively, or in addition, this rapid response could also originate
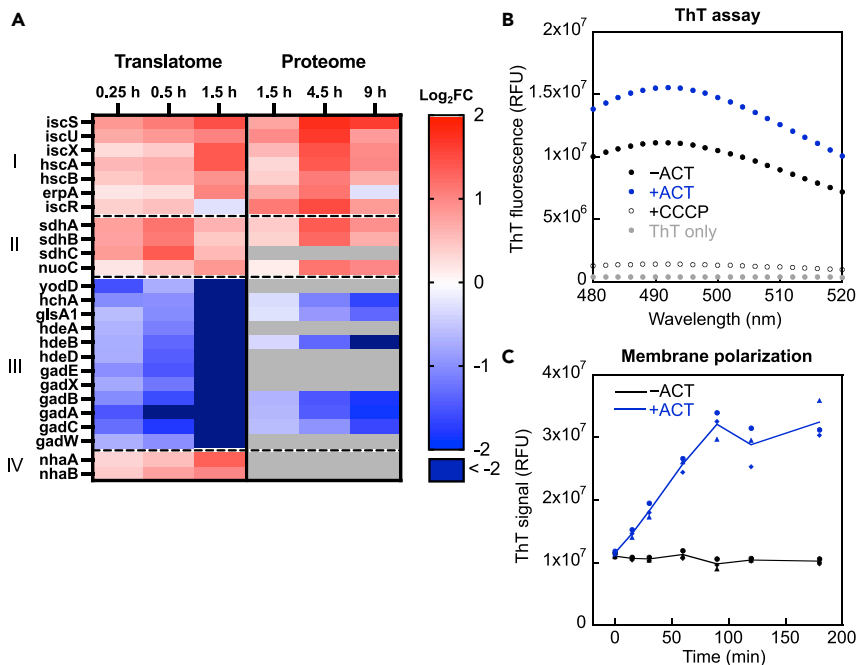
Figure 6. Inhibition of PDF induces membrane hyperpolarization

(A) Time-dependent changes ($\log_2$FC) in the translation (left) and steady-state protein level (right) of the regulated genes in the Fe-S cluster biogenesis pathway (I), the electron transfer complexes (II), the acid response pathway (III), and the alkaline response pathway (IV) upon PDF inhibition.

(B) Thioflavin T (ThT) fluorescence spectra measured with CAG12184 cells before (solid black) and after 15 min of treatment with 4 μg/mL ACT (solid blue), and after an additional 5 min of 5 μM CCCP treatment (open black). The ThT spectrum without cells is shown in gray.

(C) Membrane potential of CAG12184 cells mock-treated (black) and treated with ACT (blue), measured by the fluorescence intensity of ThT. The values for three replicates are shown, and the line represents the mean.

from the depletion of formate following PDF inhibition, as formate and tetrahydrofolate (THF) derivatives are the precursors of purines and pyrimidines (Baxter and Scott, 1984; Moffatt and Ashihara, 2002; Oizel et al., 2020). Consistent with the essential roles of formate in one-carbon metabolism (Leonhartsberger et al., 2002), we also observed changes in the translation of the genes involved in THF conversion, including glyA, metH, folA, folK, and folE (Figures 3C and S7B).

The majority of ribosomal proteins were up-regulated in the translatome after 1.5 h of ACT treatment, and their steady-state abundances started to accumulate after 4.5 h (Figure S8A). This response is likely related to the inability of several ribosomal proteins to undergo N-terminal acetylation (Cumberlidge and Isono, 1979; Jones and O'Connor, 2011; Tanka et al., 1989; Yoshikawa et al., 1987), which confer interactions to stabilize ribosome structure and modulate ribosome assembly (Clatterbuck Soper et al., 2013; Gordiyenko et al., 2008). Accordingly, multiple genes related to translation, ribosome biogenesis and rRNA modification were also up-regulated, potentially as cellular responses to rescue the ribosome assembly and translation activity (Figure S8B).

After 1.5 h of ACT treatment, we began to observe the reduced synthesis of genes involved in the energy generation pathways, such as glycolysis and the TCA cycle, and in the biosynthesis pathways for NADPH, the cellular currency for reducing power (Figure S9A). The translation of several amino acid biosynthetic pathways, which heavily depend on NADPH (Ju et al., 2020; Spaans et al., 2015), and the glutathione metabolism pathway, which plays key roles in maintaining the proper redox state of the cell (Masip et al., 2006), were down-regulated after 1.5 h of ACT treatment (Figure S9B). Accordingly, the steady-state level of multiple proteins in these pathways decreased after 4.5–9 h (Figure S9B).

To determine the role of PDF in cellular redox homeostasis, we used an established enzymatic assay to measure the levels of the different forms of nicotinamide adenine dinucleotides, which are critical electron
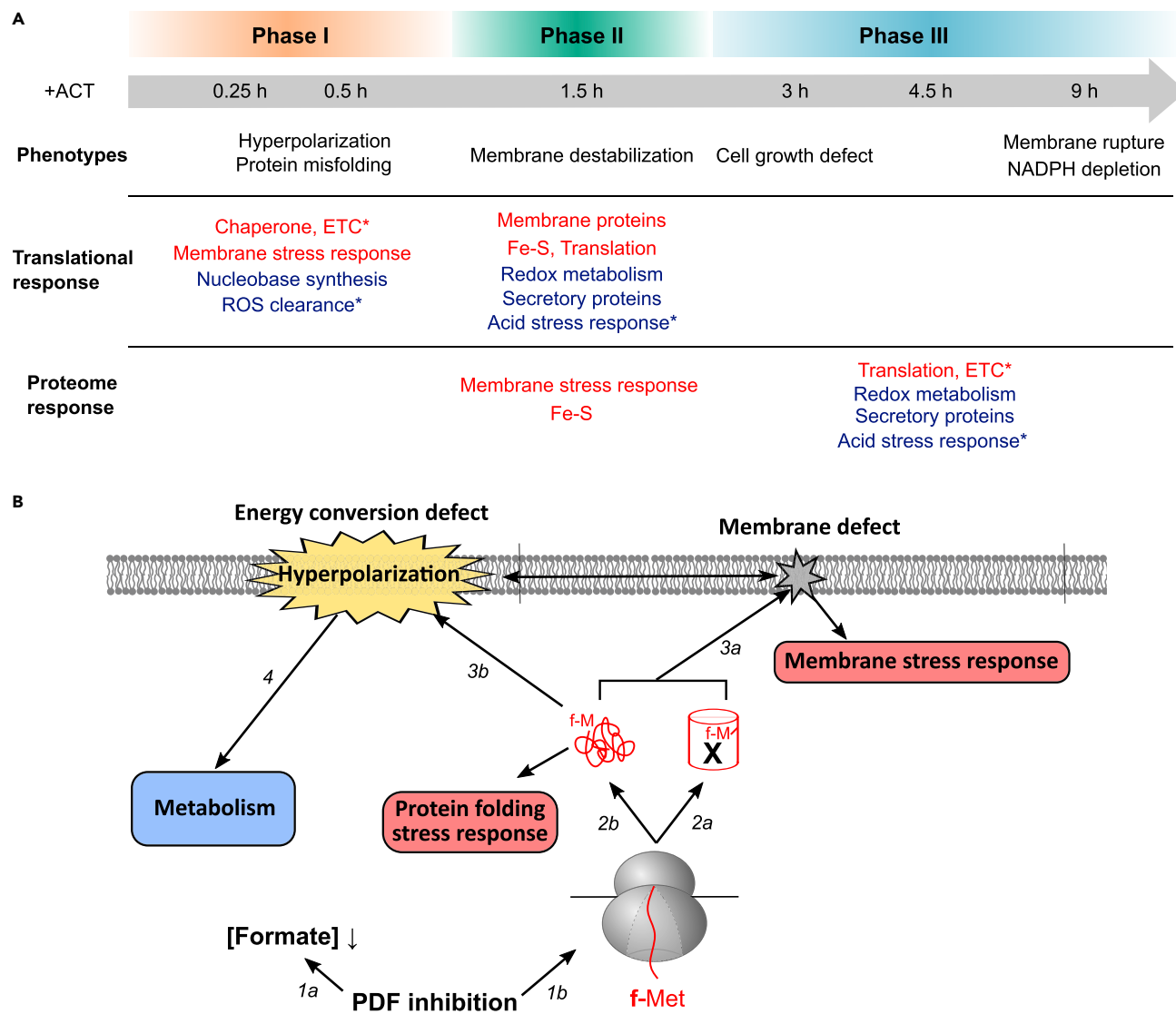
Figure 7. Impact of PDF inhibition on bacterial physiology

(A) Summary of the time-dependent changes in cell physiology, gene expression and steady state proteome level induced by PDF inhibition. Up- or down-regulated pathways in translatome or proteome are colored in red or blue, respectively. With the exception of chaperone upregulation, which turns 'off' after Phase I, all the other responses persist for the remainder of the ACT treatment. Asterisk, pathways related to oxidative phosphorylation.

(B) Model for the cellular impact of PDF inhibition, as described in the text.

carriers in metabolic reactions (Kern et al., 2014). We observed an increase in the NAD^+ levels and a depletion of NADH and NADPH after 9 h of ACT treatment, indicating an imbalance in redox homeostasis upon PDF inhibition (Figure S9C).

DISCUSSION

As the earliest covalent modifications encountered by nascent proteins, the pivotal roles of deformylation and NME are reflected by the loss of cell viability on the depletion or inhibition of PDF and MAP. However, why these modifications are essential for bacterial survival (Mazel et al., 1994) has been a long-standing question. In this work, we combined unbiased proteome and translatome analyses to investigate the roles of N-terminal protein modifications in bacterial physiology. Our results revealed different stages of cellular responses to PDF inhibition (Figure 7A). Within 15–30 min of PDF inactivation (Phase I), the cells exhibited rapid responses to protein misfolding and membrane stresses. Membrane hyperpolarization was detected

at this early stage, along with the differential translation of proteins in the ETC, which are reflected in changes in their protein levels after 1.5 h. In Phase II (1.5 h), the defect in membrane potential intensified and was accompanied by significant remodeling of the membrane proteome, including the increased synthesis of membrane proteins and reduced expression of secretory proteins. Up-regulation of the Fe-S cluster biogenesis pathway and the translation machinery also occurs at this stage, along with a reduced translation of proteins involved in multiple metabolic pathways. In Phase III (after 3 h of ACT treatment), cell growth defects are observed. The changes in the translatome during Phase II manifest in the steady-state proteome changes after 4.5 h, followed by a considerable membrane rupture and NAD(P)H depletion. These time-resolved analyses provide insights into the direct and indirect roles of PDF in regulating various biological pathways.

Multiple models could link the biochemical activity of PDF to the physiological impact of its inhibition. Proper NME is required to unmask the second residue on N-terminal nucleophile hydrolases and other enzymes (Meinnel et al., 1993). In addition, the retention of fMet may perturb the folding trajectory of nascent proteins, as the chemically similar N-terminal acetylation plays pivotal roles in controlling protein folding, targeting, and complex assembly (Aksnes et al., 2019; Forte et al., 2011; Friedrich et al., 2021; Kang et al., 2012). Our data here support the role of proper N-terminal modification in protein biogenesis. PDF inhibition leads to the formation of nascent protein aggregates and the rapid induction of heat shock responses (Figure 4). The increased translation of the membrane protein chaperone YidC and other translocation machineries also suggests membrane protein folding and translocation defects. Notably, the different biochemical mechanisms predict distinct kinetics by which PDF inhibition affects cell function. If fMet retention inhibits protein function, then defects in the function will manifest only after the turnover of pre-existing proteins that underwent the correct NME. Alternatively, if defective protein biogenesis owing to fMet retention generates toxic species that disrupt cellular functions, the defects would occur immediately after PDF inhibition. Both classes of models contribute to the cellular responses observed in our study, as discussed below.

Although PDF modifies an estimated 90% of the bacterial proteome, our time-resolved analyses suggest that the membrane is the earliest and primary target of PDF inhibition. This outcome is most strongly evidenced by the pronounced activation of membrane stress responses and membrane hyperpolarization observed in Phase I, the compromised membrane integrity, and the differential expression of multiple membrane and secretory proteins. The ACT-induced membrane defects require protein synthesis and are likely a direct consequence of fMet-retaining nascent proteins (Figures S5H, 6C, S6A, and S6D). As discussed above, the rapid onset of membrane-associated defects (<15 min) suggests that they originate from the toxicity of fMet-retaining nascent proteins that impair the mechanisms involved in maintaining membrane structure and/or function. Misfolded and aggregated proteins could disrupt membrane structure via aberrant protein-lipid interactions, as documented for amyloidogenic protein aggregates and amino-glycosides that generate mistranslated proteins (Busse et al., 1992; Davis et al., 1986; Lal et al., 2007; Sciacca et al., 2012, 2021). Alternatively, or in addition, fMet-retaining nascent proteins could interfere with the proper functioning of membrane proteins. For example, the rapid membrane hyperpolarization is most easily explained by the 'poisoning' of PMF-dissipating machinery, such as ATP synthase, ion transporters, and protein translocation machinery, many of which are up-regulated after 1.5 h of PDF inhibition. In particular, nascent membrane proteins that retain fMet may fail to translocate and thus jam or overload the translocation machinery, in analogy to the effect of N-terminal acetylation in yeast (Forte et al., 2011), leading to extensive membrane stress. The down-regulation of secretory proteins and up-regulation of various protein translocation machinery likely reflect cellular responses to reduce the load on protein translocation pathways while increasing the capacity of these pathways. Finally, the down-regulation of potassium channels (Kch, MscL, and MscS) and up-regulation of sodium transporters (ChaA, NhaA, and NhaB) (Table S3) suggest that the maintenance of selective ion gradients across the membrane is also disrupted. Regardless of the precise mechanism, the rapid onset of the membrane defects upon PDF inhibition is most consistent with models in which fMet retention generates toxic species that directly impact the structure and function of the bacterial plasma membrane.

PDF inhibition also perturbs multiple metabolic pathways in the cytoplasm. Our observations are consistent with the results of NME inhibition in archaea and higher eukaryotes, which was also reported to dysregulate glutathione metabolism and deplete NADPH (Frottin et al., 2009, 2016). Except for the down-regulation of the genes involved in THF, purine and pyrimidine biosynthesis, which is likely attributed to the role of formate as a precursor in the biosynthesis of these molecules (Baxter and Scott, 1984; Duthie

et al., 2002; Moffatt and Ashihara, 2002), the dysregulation of translation, redox metabolism and NADPH-dependent biosynthesis pathways occurred late and is likely caused by mechanisms distinct from the early-onset membrane defects. As discussed earlier, fMet retention could affect ribosome biogenesis by inhibiting the proper post-translational modifications on ribosomal proteins and impairing the activity of metabolic enzymes that rely on both PDF and MAP activity to generate key catalytic residues at the N-terminus. These effects on newly synthesized proteins manifest over time as the existing pool of proteins is replaced. However, a limited number of N-terminal nucleophilic hydrolases are known so far in E. coli (Fox et al., 2014), including PurF, asparagine synthetase B (AsnB), glutamine–fructose-6-phosphate amino-transferase (GlmS), and HslV; the small number and the redundancy of many of these proteins (Humbert and Simoni, 1980) are not sufficient to explain the extensive re-programming of metabolic pathways observed here. Alternatively, or in addition, as glycolysis and redox metabolism are intimately linked to oxidative phosphorylation at the membrane, the changes in these metabolic pathways may be a downstream effect of the dysfunctions of bioenergetics at the membrane.

Our data also help evaluate several previous models for the essentiality of NME. One model involves recycling methionine from a fraction of nascent proteins (Dummitt et al., 2003; Meinnel et al., 1993). As methionine is supplied in the growth medium and the genes involved in the methionine biosynthesis pathway are down-regulated upon PDF inhibition, increased demand for the supply of methionine is unlikely under our experimental conditions. Another potential role of fMet is to serve as a degradation signal, providing a quality control pathway for nascent proteins (Kim et al., 2018; Piatkov et al., 2015). Under our experimental conditions, however, the change in protein abundance upon PDF inhibition is primarily determined by altered protein synthesis instead of degradation. The fMet-mediated degradation is thus likely to be conditional and substrate-specific, akin to the Ac/N-degron pathway in eukaryotes (Hwang et al., 2010; Varshavsky, 2019).

We suggest the following model to explain the physiological impact of incorrect N-terminal modification in bacteria (Figure 7B). The immediate molecular consequences of PDF inhibition are the depletion of formate (Step 1a) and the accumulation of fMet-retaining nascent proteins (Step 1b). A temporary decrease in the formate level could affect the synthesis of nucleobases and one-carbon metabolism mediated by THF derivatives. However, we speculate that this effect is local, as the deformylation of nascent proteins only constitutes a fraction of the formate supply. On the other hand, nascent proteins that escape deformylation and NME immediately and profoundly affect the integrity and proper functioning of the membrane. This could occur via rapid replacement of functional proteins (Step 2a) or, more plausibly, the accumulation of misfolded protein aggregates (Step 2b), which induces protein folding stress both in the cytosol and at the membrane. Aberrant fMet-retaining proteins disrupt the structure and function of the membrane (Step 3a), including the dysregulation of PMF (Step 3b), leading to the activation of membrane stress responses as well as transcriptional/translational re-programming that adjust the demand for membrane functions, such as protein translocation and ion transport. Over time, the disruption of bioenergetics at the membrane and potential accumulation of enzymes inactivated by fMet retention leads to the down-regulation of proteins involved in redox metabolism/homeostasis and the reduction of NADPH-dependent biosynthetic pathways (Step 4).

Our work uncovers the significance of deformylation in the bacterial protein biogenesis and emphasizes the role of the inner membrane in translating the NME-linked protein biogenesis defects to cellular metabolism. Intriguingly, emerging data suggest that an intricate balance of formylation and deformylation is crucial for membrane-associated cellular functions. A previous study (Ranjan et al., 2017) and our recent work (Yang et al., 2022) demonstrated that a significant fraction of the membrane and secretory proteome is resistant to deformylation under physiological conditions, suggesting that fMet retention on some membrane and secretory proteins may be necessary. Our current work showed that the deformylation of a distinct set of the proteome is crucial for maintaining the proper structure and function of the bacterial membrane. The demand for the proper regulation of PDF activity is also observed in the eukaryotic mitochondria: the efficient assembly of the ETC complex IV requires the retention of fMet on the subunit COXI (Hinttala et al., 2015), whereas the inhibition of mitochondrial PDF leads to defects in oxidative phosphorylation (Escobar-Alvarez et al., 2010). As the deformylation reaction is sensitive to multiple factors, including protein translation and the availability of metal ions (Ragusa et al., 1998; Yang et al., 2019), we speculate that differential formylation could occur under stressed conditions. Whether and how the stress-induced remodeling of N-terminome affects cellular functions and the identity and role of the critical protein players remain outstanding goals for future investigations.

Limitations of the study

Our analyses revealed extensive cellular responses to PDF inhibition. However, as deformylation is the pre-requisite for the action of MAP, the observed phenotypes upon ACT treatment report the combined effects of the retention of N-formylation and the initiator methionine. Future studies using specific MAP inhibitors will be required further to examine the physiological roles of PDF and MAP.

STAR★METHODS

Detailed methods are provided in the online version of this paper and include the following:

- KEY RESOURCES TABLE
- RESOURCE AVAILABILITY
  - Lead contact
  - Materials availability
  - Data and code availability
- EXPERIMENTAL MODEL AND SUBJECT DETAILS
  - Bacterial strains and growth conditions
- METHOD DETAILS
  - SILAC-TMT
  - Ribosome profiling
  - Isolation of nascent protein aggregates
  - Bright field microscopy
  - SDS sensitivity assay
  - PI permeability assay
  - Membrane polarization assays
  - Measurement of $NAD(P)^+$ and $NAD(P)H$
- QUANTIFICATION AND STATISTICAL ANALYSIS
  - SILAC-TMT
  - Ribosome profiling
  - Other biochemical assays

SUPPLEMENTAL INFORMATION

Supplemental information can be found online at https://doi.org/10.1016/j.isci.2022.104756.

AUTHOR CONTRIBUTIONS

Conceptualization: C.-I.Y. and S.S.; Investigation: C.-I.Y., Z.Z., and B.L.; Formal analysis: C.-I.Y, Z.Z., and J.J.; Software: Z.Z. and J.J.; Writing – original draft: C.-I.Y; Writing – review & editing: C. -I.Y, Z.Z., J.J., B.L., T.-F.C, and S.S.; Supervision: T.-F.C, and S.S.

DECLARATION OF INTERESTS

The authors declare no competing interests.

REFERENCES

Adams, J.M. (1968). On the release of the formyl group from nascent protein. J. Mol. Biol. *33*, 571–589.

Adams, J.M., and Capecchi, M.R. (1966). N-formylmethionyl-sRNA as the initiator of protein synthesis. Proc. Natl. Acad. Sci. USA *55*, 147–155.

Aksnes, H., Ree, R., and Arnesen, T. (2019). Co-Translational, post-translational, and non-catalytic roles of N-terminal acetyltransferases. Mol. Cell *73*, 1097–1114.

Antoun, A., Pavlov, M.Y., Lovmar, M., and Ehrenberg, M. (2006). How initiation factors maximize the accuracy of tRNA selection in initiation of bacterial protein synthesis. Mol. Cell *23*, 183–193.

Barria, C., Malecki, M., and Arraiano, C.M. (2013). Bacterial adaptation to cold. Microbiology *159*, 2437–2443.

Baxter, R.L., and Scott, A.I. (1984). 1.04 - biosynthesis of some heterocyclic natural products. In Comprehensive Heterocyclic Chemistry, A.R. Katritzky and C.W. Rees, eds. (Oxford: Pergamon), pp. 83–109.

Ben-Bassat, A., Bauer, K., Chang, S.Y., Myambo, K., Boosman, A., and Chang, S. (1987). Processing of the initiation methionine from proteins: properties of the Escherichia coli methionine aminopeptidase and its gene structure. J. Bacteriol. *169*, 751–757.

Benjamini, Y., and Hochberg, Y. (1995). Controlling the false discovery rate: a practical and powerful approach to multiple testing. J. Roy. Stat. Soc. B *57*, 289–300.

Bienvenut, W.V., Giglione, C., and Meinnel, T. (2015). Proteome-wide analysis of the amino terminal status of Escherichia coli proteins at the steady-state and upon deformylation inhibition. Proteomics *15*, 2503–2518.

Brannigan, J.A., Dodson, G., Duggleby, H.J., Moody, P.C., Smith, J.L., Tomchick, D.R., and Murzin, A.G. (1995). A protein catalytic framework with an N-terminal nucleophile is capable of self-activation. Nature *378*, 416–419.

Busse, H.-J., Wöstmann, C., and Bakker, E.P. (1992). The bactericidal action of streptomycin: membrane permeabilization caused by the insertion of mistranslated proteins into the cytoplasmic membrane of Escherichia coli and subsequent caging of the antibiotic inside the cells due to degradation of these proteins. J. Gen. Microbiol. *138*, 551–561.

Chang, S.Y., McGary, E.C., and Chang, S. (1989). Methionine aminopeptidase gene of Escherichia coli is essential for cell growth. J. Bacteriol. *171*, 4071–4072.

Chen, D.Z., Patel, D.V., Hackbarth, C.J., Wang, W., Dreyer, G., Young, D.C., Margolis, P.S., Wu, C., Ni, Z.J., Trias, J., et al. (2000). Actinonin, a naturally occurring antibacterial agent, is a potent deformylase inhibitor. Biochemistry *39*, 1256–1262.

Clatterbuck Soper, S.F., Dator, R.P., Limbach, P.A., and Woodson, S.A. (2013). In vivo X-ray footprinting of pre-30S ribosomes reveals chaperone-dependent remodeling of late assembly intermediates. Mol. Cell *52*, 506–516.

Cumberlidge, A.G., and Isono, K. (1979). Ribosomal protein modification in Escherichia coli: I. A mutant lacking the N-terminal acetylation of protein S5 exhibits thermosensitivity. J. Mol. Biol. *131*, 169–189.

Davis, B.D., Chen, L.L., and Tai, P.C. (1986). Misread protein creates membrane channels: an essential step in the bactericidal action of aminoglycosides. Proc. Natl. Acad. Sci. USA *83*, 6164–6168.

Dummitt, B., Micka, W.S., and Chang, Y.-H. (2003). N-terminal methionine removal and methionine metabolism in Saccharomyces cerevisiae. J. Cell. Biochem. *89*, 964–974.

Duroc, Y., Giglione, C., and Meinnel, T. (2009). Mutations in three distinct loci cause resistance to peptide deformylase inhibitors in Bacillus subtilis. Antimicrob. Agents Chemother. *53*, 1673–1678.

Duthie, S.J., Narayanan, S., Brand, G.M., Pirie, L., and Grant, G. (2002). Impact of folate deficiency on DNA stability. J. Nutr. *132*, 2444S–2449S.

Escobar-Alvarez, S., Gardner, J., Sheth, A., Manfredi, G., Yang, G., Ouerfelli, O., Heaney, M.L., and Scheinberg, D.A. (2010). Inhibition of human peptide deformylase disrupts mitochondrial function. Mol. Cell Biol. *30*, 5099–5109.

Ezraty, B., Vergnes, A., Banzhaf, M., Duverger, Y., Huguenot, A., Brochado, A.R., Su, S.-Y., Espinosa, L., Loiseau, L., Py, B., et al. (2013). Fe-S cluster biosynthesis controls uptake of aminoglycosides in a ROS-less death pathway. Science *340*, 1583–1587.

Fieulaine, S., Boularot, A., Artaud, I., Desmadril, M., Dardel, F., Meinnel, T., and Giglione, C. (2011). Trapping conformational states along ligand-binding dynamics of peptide deformylase: the impact of induced fit on enzyme catalysis. PLoS Biol. *9*, e1001066.

Flores-Kim, J., and Darwin, A.J. (2016). The phage shock protein response. Annu. Rev. Microbiol. *70*, 83–101.

Forte, G.M.A., Pool, M.R., and Stirling, C.J. (2011). N-terminal acetylation inhibits protein targeting to the endoplasmic reticulum. PLoS Biol. *9*, e1001073.

Foster, J.W. (2004). Escherichia coli acid resistance: tales of an amateur acidophile. Nat. Rev. Microbiol. *2*, 898–907.

Fox, N.K., Brenner, S.E., and Chandonia, J.-M. (2014). SCOPe: structural Classification of Proteins—extended, integrating SCOP and ASTRAL data and classification of new structures. Nucleic Acids Res. *42*, D304–D309.

Friedrich, U.A., Zedan, M., Hessling, B., Fenzl, K., Gillet, L., Barry, J., Knop, M., Kramer, G., and Bukau, B. (2021). Nα-terminal acetylation of proteins by NatA and NatB serves distinct physiological roles in Saccharomyces cerevisiae. Cell Rep. *34*, 108711.

Frottin, F., Martinez, A., Peynot, P., Mitra, S., Holz, R.C., Giglione, C., and Meinnel, T. (2006). The proteomics of N-terminal methionine cleavage. Mol. Cell. Proteomics *5*, 2336–2349.

Frottin, F., Espagne, C., Traverso, J.A., Mauve, C., Valot, B., Lelarge-Trouverie, C., Zivy, M., Noctor, G., Meinnel, T., and Giglione, C. (2009). Cotranslational proteolysis dominates glutathione homeostasis to support proper growth and development. Plant Cell *21*, 3296–3314.

Frottin, F., Bienvenut, W.V., Bignon, J., Jacquet, E., Vaca Jacome, A.S., Van Dorsselaer, A., Cianferani, S., Carapito, C., Meinnel, T., and Giglione, C. (2016). MetAP1 and MetAP2 drive cell selectivity for a potent anti-cancer agent in synergy, by controlling glutathione redox state. Oncotarget *7*, 63306–63323.

Fujii, K., Susanto, T.T., Saurabh, S., and Barna, M. (2018). Decoding the function of expansion segments in ribosomes. Mol. Cell *72*, 1013–1020.e6.

Giglione, C., Pierre, M., and Meinnel, T. (2000). Peptide deformylase as a target for new generation, broad spectrum antimicrobial agents. Mol. Microbiol. *36*, 1197–1205.

Giglione, C., Boularot, A., and Meinnel, T. (2004). Protein N-terminal methionine excision. Cell. Mol. Life Sci. *61*, 1455–1474.

Giglione, C., Fieulaine, S., and Meinnel, T. (2015). N-terminal protein modifications: bringing back into play the ribosome. Biochimie *114*, 134–146.

Gordiyenko, Y., Deroo, S., Zhou, M., Videler, H., and Robinson, C.V. (2008). Acetylation of L12 increases interactions in the Escherichia coli ribosomal stalk complex. J. Mol. Biol. *380*, 404–414.

Greenfield, N.J., Stafford, W.F., and Hitchcock-DeGregori, S.E. (1994). The effect of N-terminal acetylation on the structure of an N-terminal tropomyosin peptide and alpha alpha-tropomyosin. Protein Sci. *3*, 402–410.

Griffith, E.C., Su, Z., Niwayama, S., Ramsay, C.A., Chang, Y.-H., and Liu, J.O. (1998). Molecular recognition of angiogenesis inhibitors fumagillin and ovalicin by methionine aminopeptidase 2. Proc. Natl. Acad. Sci. USA *95*, 15183–15188.

Gualerzi, C.O., and Pon, C.L. (1990). Initiation of mRNA translation in prokaryotes. Biochemistry *29*, 5881–5889.

Guillon, J.M., Mechulam, Y., Schmitter, J.M., Blanquet, S., and Fayat, G. (1992). Disruption of the gene for Met-tRNA(fMet) formyltransferase severely impairs growth of Escherichia coli. J. Bacteriol. *174*, 4294–4301.

Hinttala, R., Sasarman, F., Nishimura, T., Antonicka, H., Brunel-Guitton, C., Schwartzentruber, J., Fahiminiya, S., Majewski, J., Faubert, D., Ostergaard, E., et al. (2015). An N-terminal formyl methionine on COX 1 is required for the assembly of cytochrome c oxidase. Hum. Mol. Genet. *24*, 4103–4113.

Hirel, P.H., Schmitter, M.J., Dessen, P., Fayat, G., and Blanquet, S. (1989). Extent of N-terminal

methionine excision from Escherichia coli proteins is governed by the side-chain length of the penultimate amino acid. Proc. Natl. Acad. Sci. USA *86*, 8247–8251.

Hu, X., Addlagatta, A., Lu, J., Matthews, B.W., and Liu, J.O. (2006). Elucidation of the function of type 1 human methionine aminopeptidase during cell cycle progression. Proc. Natl. Acad. Sci. USA *103*, 18148–18153.

Huang, D.W., Sherman, B.T., Tan, Q., Collins, J.R., Alvord, W.G., Roayaei, J., Stephens, R., Baseler, M.W., Lane, H.C., and Lempicki, R.A. (2007). The DAVID Gene Functional Classification Tool: a novel biological module-centric algorithm to functionally analyze large gene lists. Genome Biol. *8*, R183.

Huang, D.W., Sherman, B.T., and Lempicki, R.A. (2009). Systematic and integrative analysis of large gene lists using DAVID bioinformatics resources. Nat. Protoc. *4*, 44–57.

Hudson, M.A., Siegele, D.A., and Lockless, S.W. (2020). Use of a fluorescence-based assay to measure *Escherichia coli* membrane potential changes in high throughput. Antimicrob. Agents Chemother. *64*, e00910-20.

Humbert, R., and Simoni, R.D. (1980). Genetic and biomedical studies demonstrating a second gene coding for asparagine synthetase in Escherichia coli. J. Bacteriol. *142*, 212–220.

Hwang, C.S., Shemorry, A., and Varshavsky, A. (2010). N-terminal acetylation of cellular proteins creates specific degradation signals. Science *327*, 973–977.

Ingolia, N.T., Brar, G.A., Rouskin, S., McGeachy, A.M., and Weissman, J.S. (2012). The ribosome profiling strategy for monitoring translation in vivo by deep sequencing of ribosome-protected mRNA fragments. Nat. Protoc. *7*, 1534–1550.

Jarvis, J.A., Ryan, M.T., Hoogenraad, N.J., Craik, D.J., and Høj, P.B. (1995). Solution structure of the acetylated and noncleavable mitochondrial targeting signal of rat chaperonin 10. J. Biol. Chem. *270*, 1323–1331.

Jiao, X., Sherman, B.T., Huang, D.W., Stephens, R., Baseler, M.W., Lane, H.C., and Lempicki, R.A. (2012). DAVID-WS: a stateful web service to facilitate gene/protein list analysis. Bioinformatics *28*, 1805–1806.

Jones, J.D., and O'Connor, C.D. (2011). Protein acetylation in prokaryotes. Proteomics *11*, 3012–3022.

Jovanovic, G., Mehta, P., Ying, L., and Buck, M. (2014). Anionic lipids and the cytoskeletal proteins MreB and RodZ define the spatio-temporal distribution and function of membrane stress controller PspA in Escherichia coli. Microbiology *160*, 2374–2386.

Ju, H.-Q., Lin, J.-F., Tian, T., Xie, D., and Xu, R.-H. (2020). NADPH homeostasis in cancer: functions, mechanisms and therapeutic implications. Signal Transduct. Targeted Ther. *5*, 231–312.

Käll, L., Canterbury, J.D., Weston, J., Noble, W.S., and MacCoss, M.J. (2007). Semi-supervised learning for peptide identification from shotgun proteomics datasets. Nat. Methods *4*, 923–925.

Kang, L., Moriarty, G.M., Woods, L.A., Ashcroft, A.E., Radford, S.E., and Baum, J. (2012). N-terminal acetylation of α-synuclein induces increased transient helical propensity and decreased aggregation rates in the intrinsically disordered monomer. Protein Sci. *21*, 911–917.

Kern, S.E., Price-Whelan, A., and Newman, D.K. (2014). Extraction and measurement of NAD(P)+ and NAD(P)H. In Pseudomonas Methods and Protocols, A. Filloux and J.-L. Ramos, eds. (Springer New York), pp. 311–323.

Kim, J.H., Krahn, J.M., Tomchick, D.R., Smith, J.L., and Zalkin, H. (1996). Structure and function of the glutamine phosphoribosylpyrophosphate amidotransferase glutamine site and communication with the phosphoribosylpyrophosphate site. J. Biol. Chem. *271*, 15549–15557.

Kim, J.-M., Seok, O.-H., Ju, S., Heo, J.-E., Yeom, J., Kim, D.-S., Yoo, J.-Y., Varshavsky, A., Lee, C., and Hwang, C.-S. (2018). Formyl-methionine as an N-degron of a eukaryotic N-end rule pathway. Science *362*, eaat0174.

Krulwich, T.A., Sachs, G., and Padan, E. (2011). Molecular aspects of bacterial pH sensing and homeostasis. Nat. Rev. Microbiol. *9*, 330–343.

Lal, R., Lin, H., and Quist, A.P. (2007). Amyloid beta ion channel: 3D structure and relevance to amyloid channel paradigm. Biochim. Biophys. Acta *1768*, 1966–1975.

Larsen, T.M., Boehlein, S.K., Schuster, S.M., Richards, N.G., Thoden, J.B., Holden, H.M., and Rayment, I. (1999). Three-dimensional structure of Escherichia coli asparagine synthetase B: a short journey from substrate to product. Biochemistry *38*, 16146–16157.

Leonhartsberger, S., Korsa, I., and Böck, A. (2002). The molecular biology of formate metabolism in enterobacteria. J. Mol. Microbiol. Biotechnol. *4*, 269–276.

Margolis, P.S., Hackbarth, C.J., Young, D.C., Wang, W., Chen, D., Yuan, Z., White, R., and Trias, J. (2000). Peptide deformylase in Staphylococcus aureus: resistance to inhibition is mediated by mutations in the formyltransferase gene. Antimicrob. Agents Chemother. *44*, 1825–1831.

Martin, M. (2011). Cutadapt removes adapter sequences from high-throughput sequencing reads. EMBnet J. *17*, 10–12.

Masip, L., Veeravalli, K., and Georgiou, G. (2006). The many faces of glutathione in bacteria. Antioxid. Redox Signal. *8*, 753–762.

Mazel, D., Pochet, S., and Marlière, P. (1994). Genetic characterization of polypeptide deformylase, a distinctive enzyme of eubacterial translation. EMBO J. *13*, 914–923.

Meinnel, T., Mechulam, Y., and Blanquet, S. (1993). Methionine as translation start signal: a review of the enzymes of the pathway in Escherichia coli. Biochimie *75*, 1061–1075.

Moffatt, B.A., and Ashihara, H. (2002). Purine and pyrimidine nucleotide synthesis and metabolism. Arabidopsis Book *1*, e0018.

Mohammad, F., and Buskirk, A.R. (2019). Protocol for ribosome profiling in bacteria. Bio. Protoc. *9*, e3468.

Mouilleron, S., Badet-Denisot, M.-A., and Golinelli-Pimpaneau, B. (2006). Glutamine binding opens the ammonia channel and activates glucosamine-6P synthase. J. Biol. Chem. *281*, 4404–4412.

Ninnis, R.L., Spall, S.K., Talbo, G.H., Truscott, K.N., and Dougan, D.A. (2009). Modification of PATase by L/F-transferase generates a ClpS-dependent N-end rule substrate in Escherichia coli. EMBO J. *28*, 1732–1744.

Novo, D., Perlmutter, N.G., Hunt, R.H., and Shapiro, H.M. (1999). Accurate flow cytometric membrane potential measurement in bacteria using diethyloxacarbocyanine and a ratiometric technique. Cytometry *35*, 55–63.

Oinonen, C., and Rouvinen, J. (2000). Structural comparison of ntn-hydrolases. Protein Sci. *9*, 2329–2337.

Oizel, K., Tait-Mulder, J., Fernandez-de-Cossio-Diaz, J., Pietzke, M., Brunton, H., Lilla, S., Dhayade, S., Athineos, D., Blanco, G.R., Sumpton, D., et al. (2020). Formate induces a metabolic switch in nucleotide and energy metabolism. Cell Death Dis. *11*, 310–314.

Old, I.G., Phillips, S.E., Stockley, P.G., and Saint Girons, I. (1991). Regulation of methionine biosynthesis in the enterobacteriaceae. Prog. Biophys. Mol. Biol. *56*, 145–185.

Orsburn, B.C. (2021). Proteome discoverer—a community enhanced data processing suite for protein informatics. Proteomes 9, 15.

Padan, E., Bibi, E., Ito, M., and Krulwich, T.A. (2005). Alkaline pH homeostasis in bacteria: new insights. Biochim. Biophys. Acta *1717*, 67–88.

Park, E., Lee, J.W., Eom, S.H., Seol, J.H., and Chung, C.H. (2008). Binding of MG132 or deletion of the Thr active sites in HslV subunits increases the affinity of HslV protease for HslU ATPase and makes this interaction nucleotide-independent. J. Biol. Chem. *283*, 33258–33266.

Perez-Riverol, Y., Bai, J., Bandla, C., García-Seisdedos, D., Hewapathirana, S., Kamatchinathan, S., Kundu, D.J., Prakash, A., Frericks-Zipper, A., Eisenacher, M., et al. (2022). The PRIDE database resources in 2022: a hub for mass spectrometry-based proteomics evidences. Nucleic Acids Res. *50*, D543–D552.

Piatkov, K.I., Vu, T.T.M., Hwang, C.-S., and Varshavsky, A. (2015). Formyl-methionine as a degradation signal at the N-termini of bacterial proteins. Microb. Cell *2*, 376–393.

Ping, L., Zhang, H., Zhai, L., Dammer, E.B., Duong, D.M., Li, N., Yan, Z., Wu, J., and Xu, P. (2013). Quantitative proteomics reveals significant changes in cell shape and an energy shift after IPTG induction via an optimized SILAC approach for Escherichia coli. J. Proteome Res. *12*, 5978–5988.

Prindle, A., Liu, J., Asally, M., Ly, S., Garcia-Ojalvo, J., and Süel, G.M. (2015). Ion channels enable electrical communication in bacterial communities. Nature *527*, 59–63.

R Core Team (2018). R: A Language and Environment for Statistical Computing (R Foundation for Statistical Computing). https://www.R-project.org/.

Ragusa, S., Blanquet, S., and Meinnel, T. (1998). Control of peptide deformylase activity by metal cations. J. Mol. Biol. 280, 515–523.

Ragusa, S., Mouchet, P., Lazennec, C., Dive, V., and Meinnel, T. (1999). Substrate recognition and selectivity of peptide deformylase. Similarities and differences with metzincins and thermolysin. J. Mol. Biol. 289, 1445–1457.

Ranjan, A., Mercier, E., Bhatt, A., and Wintermeyer, W. (2017). Signal recognition particle prevents N-terminal processing of bacterial membrane proteins. Nat. Commun. 8, 15562.

Ritchie, M.E., Phipson, B., Wu, D., Hu, Y., Law, C.W., Shi, W., and Smyth, G.K. (2015). Limma powers differential expression analyses for RNA-sequencing and microarray studies. Nucleic Acids Res. 43, e47.

Rohrwild, M., Coux, O., Huang, H.C., Moerschell, R.P., Yoo, S.J., Seol, J.H., Chung, C.H., and Goldberg, A.L. (1996). HslV-HslU: a novel ATP-dependent protease complex in Escherichia coli related to the eukaryotic proteasome. Proc. Natl. Acad. Sci. USA 93, 5808–5813.

Schmidt, R., Zahn, R., Bukau, B., and Mogk, A. (2009). ClpS is the recognition component for Escherichia coli substrates of the N-end rule degradation pathway. Mol. Microbiol. 72, 506–517.

Sciacca, M.F.M., Kotler, S.A., Brender, J.R., Chen, J., Lee, D.k., and Ramamoorthy, A. (2012). Two-step mechanism of membrane disruption by Aβ through membrane fragmentation and pore formation. Biophys. J. 103, 702–710.

Sciacca, M.F.M., La Rosa, C., and Milardi, D. (2021). Amyloid-mediated mechanisms of membrane disruption. Biophysica 1, 137–156.

Scott, D.C., Monda, J.K., Bennett, E.J., Harper, J.W., and Schulman, B.A. (2011). N-terminal acetylation acts as an avidity enhancer within an interconnected multiprotein complex. Science 334, 674–678.

Singer, J.M., and Shaw, J.M. (2003). Mdm20 protein functions with Nat3 protein to acetylate Tpm1 protein and regulate tropomyosin–actin interactions in budding yeast. Proc. Natl. Acad. Sci. USA 100, 7644–7649.

Singer, M., Baker, T.A., Schnitzler, G., Deischel, S.M., Goel, M., Dove, W., Jaacks, K.J., Grossman, A.D., Erickson, J.W., and Gross, C.A. (1989). A collection of strains containing genetically linked alternating antibiotic resistance elements for genetic mapping of Escherichia coli. Microbiol. Rev. 53, 1–24.

Singh, D., Majumdar, A.G., Gamre, S., and Subramanian, M. (2021). Membrane damage precedes DNA damage in hydroxychavicol treated E. coli cells and facilitates cooperativity with hydrophobic antibiotics. Biochimie 180, 158–168.

Solbiati, J., Chapman-Smith, A., Miller, J.L., Miller, C.G., and Cronan, J.E., Jr. (1999). Processing of the N termini of nascent polypeptide chains requires deformylation prior to methionine removal. J. Mol. Biol. 290, 607–614.

Spaans, S.K., Weusthuis, R.A., van der Oost, J., and Kengen, S.W.M. (2015). NADPH-generating systems in bacteria and archaea. Front. Microbiol. 6, 742.

Stocks, S.M. (2004). Mechanism and use of the commercially available viability stain. Cytometry 61, 189–195.

Sträuber, H., and Müller, S. (2010). Viability states of bacteria—specific mechanisms of selected probes. Cytometry 77, 623–634.

Sundari, R.M., Stringer, E.A., Schulman, L.H., and Maitra, U. (1976). Interaction of bacterial initiation factor 2 with initiator tRNA. J. Biol. Chem. 251, 3338–3345.

Tabb, D.L. (2015). The SEQUEST family tree. J. Am. Soc. Mass Spectrom. 26, 1814–1819.

Tanka, S., Matsushita, Y., Yoshikawa, A., and Isono, K. (1989). Cloning and molecular characterization of the generimL wich encodes an enzyme acetylating ribosomal protein L12 ofEscherichia coki K12. Mol. Gen. Genet. 217, 289–293.

Tobias, J.W., Shrader, T.E., Rocap, G., and Varshavsky, A. (1991). The N-end rule in bacteria. Science 254, 1374–1377.

Tomoyasu, T., Mogk, A., Langen, H., Goloubinoff, P., and Bukau, B. (2001). Genetic dissection of the roles of chaperones and proteases in protein folding and degradation in the Escherichia coli cytosol. Mol. Microbiol. 40, 397–413.

Tyanova, S., Temu, T., Sinitcyn, P., Carlson, A., Hein, M.Y., Geiger, T., Mann, M., and Cox, J. (2016). The Perseus computational platform for comprehensive analysis of (prote)omics data. Nat. Methods 13, 731–740.

The UniProt Consortium (2017). UniProt: the universal protein knowledgebase. Nucleic Acids Res. 45, D158–D169.

Van Aller, G.S., Nandigama, R., Petit, C.M., DeWolf, W.E., Jr., Quinn, C.J., Aubart, K.M., Zalacain, M., Christensen, S.B., Copeland, R.A., and Lai, Z. (2005). Mechanism of time-dependent inhibition of polypeptide deformylase by actinonin. Biochemistry 44, 253–260.

Varshavsky, A. (2019). N-degron and C-degron pathways of protein degradation. Proc. Natl. Acad. Sci. USA 116, 358–366.

Welle, K.A., Zhang, T., Hryhorenko, J.R., Shen, S., Qu, J., and Ghaemmaghami, S. (2016). Time-resolved analysis of proteome dynamics by Tandem mass tags and stable isotope labeling in cell culture (TMT-SILAC) hyperplexing. Mol. Cell. Proteomics 15, 3551–3563.

Yang, C.-I., Hsieh, H.-H., and Shan, S.O. (2019). Timing and specificity of cotranslational nascent protein modification in bacteria. Proc. Natl. Acad. Sci. USA 116, 23050–23060.

Yang, C.-I., Kim, J., and Shan, S.O. (2022). Ribosome-nascent chain interaction regulates N-terminal protein modification. J. Mol. Biol. 434, 167535.

Yoo, S.J., Shim, Y.K., Seong, I.S., Seol, J.H., Kang, M.-S., and Chung, C.H. (1997). Mutagenesis of two N-terminal Thr and five Ser residues in HslV, the proteolytic component of the ATP-dependent HslVU protease. FEBS Lett. 412, 57–60.

Yoshikawa, A., Isono, S., Sheback, A., and Isono, K. (1987). Cloning and nucleotide sequencing of the genes rimI and rimJ which encode enzymes acetylating ribosomal proteins S18 and S5 of Escherichia coli K12. Mol. Gen. Genet. 209, 481–488.

Zhang, D., Sweredoski, M.J., Graham, R.L.J., Hess, S., and Shan, S.O. (2012). Novel proteomic tools reveal essential roles of SRP and importance of proper membrane protein biogenesis. Mol. Cell. Proteomics 11. M111.011585.

Zhang, J., Kobert, K., Flouri, T., and Stamatakis, A. (2014). PEAR: a fast and accurate Illumina Paired-End reAd mergeR. Bioinformatics 30, 614–620.

Zhu, Z., Wang, S., and Shan, S.O. (2022). Ribosome profiling reveals multiple roles of SecA in cotranslational protein export. Nat. Commun. 13, 3393.

STAR★METHODS

KEY RESOURCES TABLE

REAGENT or RESOURCE	SOURCE	IDENTIFIER
Chemicals, peptides, and recombinant proteins		
Actinonin	Enzo	Cat#ALX-260-128-M005
$^{13}C_6$, $^{15}N_2$-L-lysine	Sigma	Cat#608041
$^{13}C_6$, $^{15}N_4$-L-arginine	Cambridge Isotope Lab	Cat#CNLM-539-H
LC/MS Grade water	Fisher	Cat#W6500
Halt protease inhibitor	Thermo Scientific	Cat#78441
Lys-C	Wako Chemicals	Cat#12505061
Trypsin	Thermo Fisher Scientific	Cat#90058
C18 Spin Column	Thermo Fisher Scientific	Cat#PI89870
DNaseI	Roche	Cat#4716728001
SUPERase·In	Ambion	Cat#AM2696
MNase	(Zhu et al., 2022)	N/A
protease inhibitor cocktail (Complete EDTA-free)	Roche	Cat#29384100
T4 polynucleotide kinase	NEB	Cat#M0201S
T4 RNA ligase 2 truncated	NEB	Cat#M0242L
Superscript III RT	Invitrogen	Cat#18080044
CircLigase	Epicentre	Cat#CL4115K
Phusion polymerase	NEB	Cat#M0530L
^{35}S-Met/Cys EasyTag mix	PerkinElmer	Cat#NEG772007MC
MG132	Sigma	Cat#474790
propidium iodide	Sigma	Cat#P4170
SYTO™ 9 Green Fluorescent Nucleic Acid Stain	Thermo Fisher Scientific	Cat#S34854
thioflavin T	Sigma	Cat#T3516
$DiOC_2(3)$	Thermo Fisher Scientific	Cat#D14730
methylthiazolyldiphenyl-tetrazolium bromide	Sigma	Cat#M2128
phenazine ethosulfate	Sigma	Cat#P4544
alcohol dehydrogenase II	Sigma	Cat#A3263
glucose-6-phosphate	Sigma	Cat#G7879
glucose-6-phosphate dehydrogenase	Sigma	Cat#10127655001
Critical commercial assays		
TMTpro 16plex reagents	Thermo Fisher Scientific	Cat#A44522
High pH Reversed-Phase Peptide Fractionation Kit	Thermo Fisher Scientific	Cat#84868
Direct-zol RNA miniprep kit	Zymo	Cat#R2050
Oligo and Concentration Kit	Zymo	Cat#D4060
Deposited data		
SILAC-TMT proteomics data	ProteomeXchange Consortium	PXD032725
Ribosome profiling data	GEO	GSE199360
Experimental models: Organisms/strains		
CAG12184	(Singer et al., 1989)	N/A
KPS73 (Δfmt)	(Piatkov et al., 2015)	N/A

(Continued on next page)

Continued		
REAGENT or RESOURCE	SOURCE	IDENTIFIER
Oligonucleotides		
Linker-1 5'-/5rApp/ NNNNNATCGTAGATCGGAAGAGCA CACGTCTGAA/3ddC/-3'	IDT, custom order	N/A
Linker-2 5'-/5rApp/ NNNNNAGCTAAGATCGGAAGAGCA CACGTCTGAA/3ddC/-3'	IDT, custom order	N/A
Linker-3 5'-/5rApp/CTGTAGGCACCATCAAT–NH2/-3'	NEB	N/A
RT-primer A 5'-/5Phos/NNAGATCGGAAGAGCGTCGTGTAGGGAAAGAG/iSp18/GTG ACTGGAGTTCAGACGTGTGCTC-3'	IDT, custom order	N/A
RT-primer B 5'-/5Phos/GATCGTCGGACTGTAGAACTCTGAACCTGTCGGTGGTCGCC GTATCATT/iSp18/CACTCA/iSp18/CAAGCAGAAGACGGCATACGAATTG ATGGTGCCTACAG-3'	IDT, custom order	N/A
PCR forward primer A 5'-AATGATACGGCGACCACCGAGATCTACACTCTTTCCCTACACGAC GCTC-3'	IDT, custom order	N/A
PCR forward primer B 5'-AATGATACGGCGACCACCGAGATCTACAC-3'	IDT, custom order	N/A
Barcoded PCR reverse primer 5'-CAAGCAGAAGACGGCATACGAGATJJJJJJGTGACTGGAGTTCAGA CGTGTGCTCTTCCG-3'	IDT, custom order	N/A
Software and algorithms		
Proteome Discoverer 2.5	Thermo Scientific (Orsburn, 2021)	N/A
R v 3.0.2	The R Foundation	https://www.r-project.org/
R::limma package	(Ritchie et al., 2015)	http://www.bioconductor.org
DAVID Bioinformatics Resources 6.8	(Jiao et al., 2012)	https://david.ncifcrf.gov/
PEAR	(Zhang et al., 2014)	https://cme.h-its.org/exelixis/web/ software/pear/
Cutadapt	(Martin, 2011)	https://github.com/marcelm/cutadapt
Perseus v 1.6.14.0	(Tyanova et al., 2016)	https://maxquant.net/perseus/
All original code	ProteomeXchange Consortium	PXD032725

RESOURCE AVAILABILITY

Lead contact

Further information and requests for resources and reagents should be directed to and will be fulfilled by the lead contact, Shu-ou Shan (sshan@caltech.edu).

Materials availability

This study did not generate new unique reagents.

Data and code availability

- The mass spectrometry proteomics data have been deposited to the ProteomeXchange Consortium via the PRIDE (Perez-Riverol et al., 2022) partner, and the ribosome profiling data is available at GEO. The data are publicly available as of the date of publication. Accession numbers are listed in the key resources table.

- All original code has been deposited to the ProteomeXchange Consortium and is publicly available as of the date of publication. The accession number is listed in the key resources table.

- Any additional information required to reanalyze the data reported in this paper is available from the lead contact upon request.

EXPERIMENTAL MODEL AND SUBJECT DETAILS

Bacterial strains and growth conditions

SILAC-TMT

E. coli cells from strain CAG12184 (Singer et al., 1989) were grown at 37°C in SILAC medium (48 mM Na_2HPO_4, 22 mM KH_2PO_4, 8 mM NaCl, 19 mM NH_4Cl, 2 mM $MgSO_4$, 0.1 mM $CaCl_2$, 0.4% glucose, 10 µg/mL tetracyclin, 40 µg/mL each of Ser, Thr, Val, Phe, Ile, Leu, Tyr, His, Met, Trp, Lys, and Arg) for optimal metabolic labeling of Lys and Arg isotopes (Ping et al., 2013). For SILAC experiments, two parallel cultures were grown in the presence of light or heavy Lys ($^{13}C_6$, $^{15}N_2$-*L*-lysine, Sigma) and Arg ($^{13}C_6$, $^{15}N_4$-*L*-arginine, Cambridge Isotope Lab) for >30 generations to allow ≥95% incorporation of the isotope labels. At OD_{600} = 0.4, 4 µg/mL ACT (Enzo) was added to the light culture. Cells were continuously diluted with fresh medium with or without ACT whenever the OD_{600} reached 0.6-0.8. At indicated time points, cells were harvested by centrifugation and flash-frozen in liquid nitrogen. Three parallel experiments (Replicate 1-3) and one independent measurement (Replicate 4) were carried out for a total of 4 biological replicates.

Ribosome profiling

E. coli CAG12184 cells were grown in SILAC medium at 37°C and treated with 4 µg/mL ACT when OD_{600} reached 0.4. Cells were continuously diluted with fresh medium with or without ACT whenever the OD_{600} reached 0.6-0.8. At indicated time points, 200 mL of cell culture were harvested by rapid filtration through nitrocellulose membrane with 0.2 mm pores and flash-frozen in liquid nitrogen. Two parallel experiments (Replicate 1 and 2) and a third independent measurement (Replicate 3) were carried out for a total of 3 biological replicates.

Other biochemical assays

Where indicated, CAG12184 or Δfmt (Piatkov et al., 2015) cells grown in SILAC medium or Luria-Bertani Broth (LB) were grown at 37°C with shaking to an OD_{600} of 0.4 and mock-treated or treated with 4 µg/mL ACT. Cells were continuously diluted with fresh medium with or without ACT whenever the OD_{600} reached 0.6-0.8.

METHOD DETAILS

SILAC-TMT

MS sample preparation

All of the buffers were made using LC/MS Grade water (Fisher). Cells were resuspended with MS buffer (50 mM Hepes-NaOH, pH 8.5) containing 10 M urea and 1X Halt protease inhibitor (Thermo Scientific), sonicated briefly, and centrifuged (16,600 × *g*, 5 min) at room temperature to remove cell debris. The lysate was diluted to reduce the urea concentration to 8 M, and the protein concentration was determined by Bradford assay (Bio-rad). An equal amount of total proteins from heavy and light isotope-labeled cells were mixed, reduced by 10 mM TCEP (20 min incubation at room temperature), and alkylated by 27 mM 2-chloroacetamide (15 min incubation in dark at room temperature). Lys-C (Wako Chemicals) was added to the sample at an enzyme-to-protein ratio of 1:200, and incubated at 37°C for 4 h. The sample was further diluted with MS buffer to reduce the urea concentration to 2 M, and incubated overnight with trypsin (Thermo Fisher Scientific) at an enzyme-to-protein ratio of 1:100. The digested peptides were then acidified with 0.5% trifluoroacetic acid (TFA), and desalted with C18 Spin Columns (Thermo Fisher Scientific). For SILAC-TMT experiment, desalted peptides were further labeled with TMTpro 16plex reagents (Thermo Fisher Scientific). An equal amount of peptides with different TMT labels were pooled, desalted, and separated into 8 fractions using High pH Reversed-Phase Peptide Fractionation Kit (Thermo Fisher Scientific).

LC-MS analysis of SILAC-TMT samples

LC-MS analysis was carried out on an EASY-nLC 1200 (Thermo Fisher Scientific) coupled to an Orbitrap Eclipse mass spectrometer (Thermo Fisher Scientific) equipped with a Nanospray Flex ion source. Peptides (500ng per fraction) were directly loaded onto an Aurora 25cm x 75µm ID, 1.6µm C18 column (Ion Opticks, Victoria, Australia) heated to 50°C. The peptides were separated with a 120 min gradient at a flow rate of 350 nL/min as follows: 2–6% Solvent B (7.5 min), 6–25% B (82.5 min), 25–40% B (30 min), 40–98% B (1 min),

and held at 98% B (15 min). Solvent A consisted of 97.8% H_2O, 2% ACN, and 0.2% formic acid and solvent B consisted of 19.8% H_2O, 80% ACN, and 0.2% formic acid. MS1 spectra were acquired in the Orbitrap at 120K resolution with a scan range from 350–1800 m/z, an AGC target of $1e^6$, and a maximum injection time of 50 ms in Profile mode. Features were filtered for monoisotopic peaks with a charge state of 2-7 and minimum intensity of $2.5e^4$, with dynamic exclusion set to exclude features after 1 time for 30 s with a 5-ppm mass tolerance. A targeted mass difference selection node was also used to monitor for SILAC pairs with a delta mass of 8.0142 Da (Lysine-8) or 10.008 Da (Arginine-10) and trigger both precursors of the SILAC pair for MS2 analysis. HCD fragmentation was performed with fixed collision energy of 32% after quadrupole isolation of features using an isolation window of 0.5 m/z, an AGC target of $5e^4$, and a maximum injection time of 86 ms. MS2 scans were then acquired in the Orbitrap at 50K resolution in Centroid mode with the first mass fixed at 110. Cycle time was set at 3 s.

Ribosome profiling

Cell lysis and ribosome footprint preparation

Frozen cells were mixed with 0.5 mL of Lysis buffer (50 mM Hepes-KOH, 100 mM NaCl, 10 mM $MgCl_2$, 5 mM $CaCl_2$, 0.4% Triton X-100, 0.1% NP-40, 1 mM chloramphenicol, 1 mM PMSF, 50 U/mL DNaseI (recombinant DNaseI, Roche), pH 7.0) and lysed via mixer milling (1 min, 25 Hz, Retsch). Frozen lysate powder was thawed and centrifuged (3,000 × g, 6 min, 4°C) to remove unbroken cells. Lysate containing 0.5 mg total RNA was supplemented with 100 U/mL SUPERase·In (Ambion), and treated with 1875 U of MNase for 15 min in a thermomixer (1,400 rpm, 25°C) before quenching with 6 mM EGTA. Monosomes were then loaded on a 30% sucrose cushion in Wash buffer (50 mM Tris/HCl, 150 mM NaCl, 10 mM $MgCl_2$, 1 mM chloramphenicol, 0.4% Triton X-100, 0.1% NP-40, pH 7.4) containing 1X protease inhibitor cocktail (Complete EDTA-free, Roche), and centrifuged in TLA100.3 rotor at 80,000 rpm for 1.5 h at 4°C. Pellets were then washed and resuspended in Wash buffer. RNA from the purified monosomes were extracted using Direct-zol RNA mini-prep kit (Zymo) and loaded onto a 15% polyacrylamide TBE-Urea gel. The 15-45 nt region on the gel was excised, and ribosome protected mRNA footprints were recovered from the gel pieces, precipitated, and resuspended in 4 μL of 10 mM Tris/HCl (pH 8.0).

Library preparation

Libraries are prepared as described (Mohammad and Buskirk, 2019; Zhu et al., 2022) with modifications. For dephosphorylation, 3.5 μL of mRNA fragments was denatured for 2 min at 80°C followed by quick cooling on ice, mixed with 0.5 μL 10X T4 polynucleotide kinase buffer (NEB), 0.5 μL T4 polynucleotide kinase (NEB) and 0.5 μL SUPERase·In, and incubated for 1 h at 37°C. For linker ligation, 3.5 μL 50% w/v PEG-8000, 0.5 μL 10x T4 RNA ligase 2 buffer (NEB), 0.5 μL 20 μM pre-adenylated linkers (Linker-1, Linker-2, and Linker-3 for replicate 1, replicate 2, and replicate 3, respectively), and 0.5 μL T4 RNA ligase 2 truncated (NEB) were added into each sample and incubated for 3 h at 30°C. Ligated products were purified with Oligo and Concentration Kit (Zymo), and samples from replicate 1 and 2 were pooled. Products were separated from excess linkers on a 15% polyacrylamide TBE-Urea gel, extracted from the gel pieces, and resuspended in 10 μL of nuclease-free H_2O. Reverse transcription was subsequently carried out by adding 4 μL 5x RT buffer (Invitrogen), 2 μL 1.25 μM RT-primer A for the pooled replicate 1 and 2 or RT-primer B for replicate 3,1 μL 10 mM dNTPs, 1 μL 0.1 M DTT, 1 μL SUPERase·In and 1 μL Superscript III RT (Invitrogen). The reaction was incubated for 30 min at 50°C, followed by addition of 2.3 μL of 1 M NaOH and incubation for 20 min at 70°C to hydrolyze the RNA fragments. Reverse-transcribed DNA products were further purified on a 10% polyacrylamide TBE-Urea gel to remove excess RT primers, extracted using DNA extraction buffer (300 mM NaCl, 1 mM EDTA, 10 mM Tris/HCl, pH 8.0), and resuspended in 15 μL of 10 mM Tris/HCl (pH 8.0). For circularization, 2 μL 10X CircLigase buffer (Epicentre), 1 μL 1 mM ATP, 1 μL 50 mM $MnCl_2$ and 1 μL CircLigase (Epicentre) were added and incubated for 1h at 60°C, followed by an additional incubation at 80°C for 10min to inactivate the enzyme. Circularized DNA was amplified via 5-8 cycles of PCR reaction using Phusion polymerase (NEB), barcoded PCR Reverse primer, and PCR Forward primer A for the pooled replicate 1 and 2 or PCR Forward primer B for replicate 3. The DNA products were purified on a 8% polyacrylamide native TBE gel, and then quantified by Qubit.

Isolation of nascent protein aggregates

E. coli CAG12184 cells grown in SILAC medium at 37°C until OD_{600} reached 0.4. Subsequently, the cells were labeled with 10 μCi/mL ^{35}S-Met/Cys EasyTag mix (PerkinElmer) and, where indicated, treated with 4 μg/mL ACT and 20 μM MG132 (Sigma) for 30 min. Before harvesting, 0.5 mg/mL Met and Cys was added

to the culture. Cells from 5 mL of culture were pelleted, resuspended in 250 μL Lysis buffer B (100 mM Hepes-KOH, 0.25 M sucrose, 0.5 mM EDTA, 50 μg/mL lysozyme, 1 mM PMSF, 1X protease inhibitor cocktail, 20 μM MG132, pH 7.0), and lysed by tip sonication (Branson, 20x at level 5 and 50% duty cycle). Lysates were centrifuged at 2,000 × g and 4°C for 5 min to remove unbroken cells. Clarified lysates were centrifuged at 15,000 × g and 4°C for 30 min to separate the membrane fraction and aggregates from cytoplasm. The pellets were further resuspended in 200 μL Wash buffer B (100 mM Hepes-KOH, 1 mM PMSF, 1X protease inhibitor cocktail, pH 7.0) with brief sonication. To isolate large protein aggregates, 2% NP-40 was added, and the resuspended pellets were centrifuged again at 15,000 × g, 4°C for 30 min. NP-40 insoluble protein aggregates were then resuspended in 50 μL Wash buffer B with 1% SDS. All fractions were then analyzed by SDS/PAGE and quantified by autoradiography.

Bright field microscopy

CAG12184 cells grown in SILAC medium were treated with 4 μg/mL ACT, collected at indicated time points, washed, and resuspended with PBS to an OD of 1. 2 μL of the cell suspension was spotted onto an agarose (1%)-coated glass slide, and covered with a glass coverslip. Bright field microscopy images were obtained with Revolve Microscope (Echo) with a 100x oil immersion objective.

SDS sensitivity assay

CAG12184 cells grown in SILAC medium to an OD_{600} of 0.4 were mock-treated or treated with 4 μg/mL ACT. At indicated time points, an aliquot of cells was pelleted, resuspended with SILAC medium to an OD_{600} of 1, and mixed with equal volume of 0.1% SDS. Cell lysis was monitored on a plate reader continuously for 20 min by the change in OD_{600} value relative to that of the cells without SDS incubation. For Figure 5B, the fraction of remaining cells at 10 min of SDS incubation was recorded.

PI permeability assay

Where indicated, CAG12184 or Δfmt (Piatkov et al., 2015) cells grown in SILAC medium or Luria-Bertani Broth (LB) were mock-treated or treated with 4 μg/mL ACT at an OD_{600} of 0.4. At indicated time points, an aliquot of cells were withdrawn, washed, and resuspended in PI buffer (50 mM Hepes-KOH, 5 mM glucose, pH 7.0) to an OD of 0.5. Resuspended cells were incubated with 5 μM PI for 30 min, and the fluorescence signals were recorded using a plate reader with the excitation wavelength at 535 nm. Independent cell resuspensions were incubated with 2.5 μM Syto9, and the fluorescence signals were measured with the excitation wavelength at 440 nm. The fluorescence intensity of PI at 620 nm was then normalized to that of Syto9 at 505 nm.

Membrane polarization assays

CAG12184 grown in SILAC medium or Δfmt cells grown in LB were treated with 4 μg/mL ACT at an OD_{600} of 0.4. Where indicated, cells were treated with 5 μM CCCP for 5 min before collection. At indicated time points after ACT treatment, cells were withdrawn, washed with PBS, and normalized to an OD_{600} of 0.5. Resuspended cells were incubated with 10 μM ThT at room temperature for 5 min, and the fluorescence signals were recorded using a plate reader at the excitation wavelength of 450 nm.

For measurements using $DiOC_2(3)$, cells were collected, resuspended to an OD_{600} of 1 with PBS, and treated with 10 mM EDTA for 5 min. The cell suspension was then washed and resuspended in MP buffer (130 mM NaCl, 60 mM Na_2HPO_4, 60 mM NaH_2PO_4, 10 mM glucose, 5 mM KCl, 0.5 mM $MgCl_2$, pH 7.0). The cell suspension was loaded with 30 μM $DiOC_2(3)$ and incubated at room temperature for 15 min, followed by fluorescence measurement with an excitation wavelength of 450 nm.

Measurement of NAD(P)$^+$ and NAD(P)H

The cellular concentrations of NAD(P)$^+$ and NAD(P)H were measured as described (Kern et al., 2014). Briefly, CAG12184 cells grown in SILAC medium were treated with 4 μg/mL ACT for 9 h. Cell aliquots were withdrawn, pelleted, and incubated at 50°C for 10 min in 0.2 M NaOH for NAD(P)$^+$ or 0.2 M HCl for NAD(P)H extraction. The lysate was then neutralized and clarified by centrifugation at 16,000 × g, 4°C for 5 min. For NAD$^+$ and NADH measurements, 5 μL of the lysate was incubated at 30°C for 10 min with 90 μL of the reagent mix containing 110 mM bicine buffer (pH 8.0), 11% (v/v) ethanol, 4.4 mM EDTA, 0.47 mM MTT (methylthiazolyldiphenyl-tetrazolium bromide), and 3.7 mM PES (phenazine ethosulfate). 5 μL of 1 mg/mL Alcohol dehydrogenase II (ADH II, Sigma) was added to initiate the reaction, and the

absorbance at 570 nm was monitored for 20 min at 30°C in a plate reader. NADP$^+$ and NADPH measurements were carried out similarly, except that ethanol in the reagent mix was replaced with 2.8 mM glucose-6-phosphate, and 5 μL of 0.1 mg/mL Glucose-6-phosphate dehydrogenase (Sigma) was used to initiate the reaction. The velocities of the reactions were normalized by cell density, and the relative amount of NAD(P)(H) was reported as the ratio of the normalized values between ACT-treated and untreated samples.

QUANTIFICATION AND STATISTICAL ANALYSIS

SILAC-TMT

Data reduction and statistical analysis

Analysis of LCMS proteomic data was performed in Proteome Discoverer 2.5 (Thermo Scientific) (Orsburn, 2021) utilizing a dynamic modification strategy to account for the TMT/SILAC mixed labeling, with the peptide results ported to R (R Core Team, 2018) for final analysis. All searches were conducted using the Sequest HT (Tabb, 2015) search algorithm with the *Escherichia coli* proteome (UniProt UP000000625; strain K12 / MG1655 / ATCC 47076; 4,438 proteins covering 440 genes with a BUSCO assessment of 100% genetic coverage). Search parameters were as follows: fully tryptic protease rules with 2 allowed missed cleavages, precursor mass tolerance set to 20 ppm, fragment mass tolerance set to 0.5 Da with only b and y ions accounted for. Percolator (Käll et al., 2007) was used as the validation method, based on q-value, with a maximum FDR set to 0.01. The SequestHT search considered modifications dynamic for Loss of Protein N-term Methionine, Formylation (N-term), Oxidation (M), Carbamidomethyl (C), TMTpro (K, N-term, +304.207 Da), TMTpro-SILAC-K8 (K, +312.221 Da) and SILAC-R10 (R, +10.008 Da). Quantitative analysis is based on TMT MS2 reporter ions generated from HCD fragmentation, with an average reporter S/N threshold of 10.

Peptide data was divided into *light-only* (not containing a SILAC modification) and *heavy-only* (containing a SILAC modification) with normalization accomplished using the R::limma package (Ritchie et al., 2015). Peptides from the two datasets where then merged such that all peptides from the *light-only* dataset had a corresponding *heavy-only* peptide, for a total of 32 TMT (16 *light-only*, 16 *heavy-only*) quantitative measurements per peptide. Protein values were calculated as the sum of each TMT channel for all corresponding peptides, with time-dependent foldchange (FC_t) values computed as all pairwise combinations between time points ($t1.5h/t0h$, $t4.5h/t0h$, $t9h/t0h$), within the light and heavy data sets independently, for a total of 16 FC_t values per comparison. FC_t values were additionally log2 transformed. Statistical analyses were performed in R using a two-sample t-test (Benjamini and Hochberg, 1995), in which the difference between the *light-only* (treated) $\log_2 FC_t$ value and the *heavy-only* (untreated) $\log_2 FC_t$ value is defined as $\log_2 FC$. Significance was determined at an adjusted p-value of 0.05 and a threshold of $|\log_2 FC| \geq 0.5$ for 1.5 h, $|\log_2 FC| \geq 1$ for 4.5 and 9 h samples.

Enrichment analysis

Enrichment analysis was performed on differentially expressed genes at each time point using the Functional annotation clustering algorithm from DAVID Bioinformatics Resources 6.8 (Jiao et al., 2012) with the 1932 identified proteins as the background. The analysis was performed with medium classification stringency and included the following annotation categories: Gene Ontology (GO) terms (biological process, molecular function, cellular component), Uniprot Keywords and Sequence features, KEGG pathway, and protein domains (InterPro, SMART, and PIR SuperFamily).

Ribosome profiling

Sequencing data analysis

The DNA library for the ribosome protected mRNA footprints was sequenced on Nextseq 2000. Pair-end reads were merged using PEAR (Zhang et al., 2014). Adaptor sequences were trimmed from sequencing reads using Cutadapt (Martin, 2011). Reads were mapped to bacterial genome using Bowtie after discarding the reads mapping to ribosomal RNAs. The *E.coli* MG1655 reference genome assembly (ASM584v2) was downloaded from EnsemblBacteria (https://bacteria.ensembl.org). Ribosome density was assigned to 14-nt upstream of the 3′-end of reads using reads with size range 15–45 nt. Nucleotide reads at each codon were then summed based on the gene annotations taken from Uniprot (The UniProt Consortium, 2017). For each gene, the sum of raw reads and RPM-normalized reads at each codon, excluding the first five and last five codons, were calculated. In each replicate, genes with ≥ 64 raw reads in the control sample

and ≥ 64 raw reads in at least one of the 3 time points were considered. The fold change (FC) was calculated as the ratio of the RPM value of ACT-treated samples at each time point to that of the sample before the addition of ACT. Genes with at least 2 valid $\log_2$ FC values from 3 replicates were included in subsequent analyses.

Statistical analysis

Statistical analyses were performed using the two-sample t-test embedded in the Perseus software (version 1.6.14.0) (Tyanova et al., 2016). Significance was determined with thresholds of $|\log_2 FC| \geq 1$ and $p < 0.05$.

Enrichment analysis

Enrichment analysis was performed on differentially expressed genes at each time point using the Functional annotation clustering algorithm from DAVID Bioinformatics Resources 6.8 (Jiao et al., 2012) with the 2405 identified genes as the background, as described for the proteomic analysis.

Other biochemical assays

Statistical analyses of protein aggregation and NAD(P)(H) assays were performed using Student's t tests. Data for each experiment were acquired from three biological replicates. A p-value of less than 0.05 was considered to be statistically significant.